JGR Solid Earth

RESEARCH ARTICLE
10.1029/2019JB018844

Key Points:
- This study explores the capability of bonded block models to replicate the prepeak and postpeak attributes of a granitic rock
- The model exhibited a degradation of specimen-scale cohesion and mobilization of friction angle with increase in damage
- Two-dimensional digital image correlation analysis was conducted on the model results to evaluate the changes in strain field

Correspondence to:
S. Sinha,
sankhaneelsinha@mymail.mines.edu

Citation:
Sinha, S., Shirole, D., & Walton, G. (2020). Investigation of the micromechanical damage process in a granitic rock using an inelastic bonded block model (BBM). *Journal of Geophysical Research: Solid Earth*, *124*. https://doi.org/10.1029/2019JB018844

Received 7 OCT 2019
Accepted 11 MAR 2020
Accepted article online 16 MAR 2020

Investigation of the Micromechanical Damage Process in a Granitic Rock Using an Inelastic Bonded Block Model (BBM)

S. Sinha[1], D. Shirole[2], and G. Walton[1]

[1]Department of Geology and Geological Engineering, Colorado School of Mines, Golden, CO, USA, [2]Department of Civil and Environmental Engineering, Colorado School of Mines, Golden, CO, USA

Abstract This study numerically investigates the damage process in a granite using an inelastic multiminerallic block model in two-dimensional Universal Distinct Element Code. In addition to the commonly considered calibration targets like uniaxial and triaxial strengths, tensile strength, and Young's modulus, attention was paid to reproduce additional attributes such as postpeak response, residual strengths, and confinement-dependent dilatancy to minimize the nonuniqueness potential of the models. The fracture pattern transitioned from axial cracking to shear banding as the specimen confinement was increased from 0 to 60 MPa. Most notably, the model could exhibit the cohesion-weakening-frictional-strengthening behavior that is typically associated with brittle rocks. The progressive damage mechanism in the unconfined bonded block model (BBM) was subsequently studied using the 2-D digital image correlation (2-D-DIC) approach. To date, the application of the 2-D-DIC approach has been restricted only to real material testing; this study, therefore, is an attempt to extend its applicability to numerical models. It was found that 2-D-DIC is capable of imaging the simulated microcracking process very well and the results were similar to those observed from real testing on a different granitic rock. Lastly, the numerical-based DIC results were analyzed to clarify that even if the point of axial stress-axial strain nonlinearity does not coincide with the point of volumetric strain reversal in unconfined BBMs, the axial stress-axial strain nonlinearity approach should always be used for determining the crack damage threshold in BBMs.

1. Introduction

Grain-scale heterogeneity in brittle rocks plays an important role in controlling its emergent macroscopic response under compression (Farahmand & Diederichs, 2015; Lan et al., 2010; Wong et al., 2006). Micromechanical observations during testing (Brace et al., 1966; Fairhurst & Cook, 1966; Martin & Chandler, 1994; Sprunt & Brace, 1974; Tapponnier & Brace, 1976) and numerical studies (Farahmand & Diederichs, 2015; Peng et al., 2018) have been used to identify that the initial mode of crack formation is in tension, which later transitions to a shear mode as cracks begin to interact. The stress levels at which the tensile and shear cracks initiate are referred to as the crack initiation (CI) and crack damage (CD) thresholds, respectively (Diederichs, 2003; Diederichs & Martin, 2010; Martin & Chandler, 1994). It is generally accepted that heterogeneity (geometric and stiffness) is responsible for the generation of the local tensile stress concentrations that cause damage initiation at CI (Blair & Cook, 1998a, 1998b; Dey & Wang, 1981; Gallagher et al., 1974). Beyond CD, previously isolated microcracks begin to interact and propagate, and this process eventually leads to the failure of the specimen via axial cracking (unconfined/low confinement conditions) or shear band formation (under confined conditions; Bieniawski, 1967; Eberhardt et al., 1999; Martin & Chandler, 1994).

At the grain scale, the microcracking process in unconfined and confined compression tests is somewhat different. When the specimen is unconfined, cracking primarily occurs along grain boundaries, as these are inherent points of weakness in the rock microstructure. Under confined conditions, however, due to geometrical interlocking and mobilization of frictional forces along the grain boundaries, damage occurs both through grain-boundary cracking and crushing and shearing within the grains (intragranular fracturing; Abdelaziz et al., 2018; Eberhardt et al., 1999; Haimson & Chang, 2000; Hofmann et al., 2015; Lee et al., 2006; Peng et al., 2018; Sprunt & Brace, 1974; Tapponnier & Brace, 1976; Wong, 1982).

From a macroscopic perspective, as damage evolves in brittle rocks, the cohesional and frictional components of strength do not degrade simultaneously. Martin and Chandler (1994) illustrated through laboratory testing on Lac du Bonnet Granite that it is the cohesional strength that degrades first, followed by friction mobilization. Hajiabdolmajid et al. (2002) later developed the cohesion-weakening-frictional-strengthening (CWFS) model for this behavior, and this model has since then been used to characterize various rock types (Walton, 2014, 2018; Walton & Diederichs, 2015b).

While laboratory testing has historically been the primary approach for studying micromechanical damage processes in brittle rock, recent years have seen a rapid rise in the use of advanced numerical modeling tools (Abdelaziz et al., 2018; Chen et al., 2016; Lan et al., 2010; Liu et al., 2018; Villeneuve et al., 2009; Zhou et al., 2019). Such models are convenient for study of certain aspects of physical processes that are difficult (or impossible) to study through laboratory testing. A model calibrated to limited laboratory data also provides the opportunity to test and evaluate potential system behaviors under a wide variety of different conditions. For example, a reliable micromechanical model of a granite calibrated to laboratory data could be potentially used to evaluate the effects of grain shape and size on damage processes, strength, and deformation characteristics. Since the accuracy of such analyses is highly dependent on the extent to which various physical phenomena are reproduced by the model used, it is important to continue to improve modeling approaches. This study is such an attempt to advance the laboratory-scale numerical representation of damage and deformation processes in granitic rocks.

In terms of simulating the rock fracturing process, numerical modeling techniques can be broadly subdivided into two groups—continuum and discontinuum. Continuum models implicitly represent the strain-weakening process by allowing the elements to yield in an inelastic manner (Chen et al., 2007; Li et al., 2003; Villeneuve et al., 2009; Zhu & Tang, 2004). The evolution of damage in such cases is controlled primarily by the constitutive relationships assigned to the elements. Alternatively, explicit simulation of the microcrack growth and coalescence process can be achieved either through the use of the discrete element method or the finite-discrete element method, both of which are physics-based models that allow the formation of true discontinuum fractures (Cundall, 1971; Mahabadi, 2012; Munjiza, 2004). This study is focused on the bonded block modeling (BBM) approach for the study of intact rock damage, which is implemented using discrete element method (Ghazvinian et al., 2014; Itasca, 2014; Kazerani & Zhao, 2010; Lan et al., 2010).

BBMs represent a material space as an aggregate of polygonal or triangular blocks that interact with each other through their contacting interfaces. The contacts fail when the shear stress or the normal stress acting on them exceeds the shear strength or the tensile strength, respectively (Itasca, 2014). In laboratory-scale models, the blocks can be considered to represent the mineral grains in a rock, and the interfaces between the blocks correspond to grain boundaries. While both polygonal and triangular BBMs have been used for simulating small (Farahmand & Diederichs, 2015; Gao et al., 2016; Gao & Stead, 2014; Lan et al., 2010) and large (excavation) scale (Bai et al., 2016; Christianson et al., 2006; Farahmand et al., 2018; Gao & Stead, 2014) damage processes in rocks, polygonal blocks (generated as a Voronoi Tessellation) are preferred for modeling granites due to the closer resemblance in shape of the unit blocks to actual mineral grains (Gao et al., 2016; Ghazvinian et al., 2014; Li et al., 2019).

Voronoi BBMs are often developed in the Itasca software Universal Distinct Element Code (UDEC; Itasca, 2014). Each of the polygonal blocks in UDEC can be considered to be either rigid or deformable; if deformable, the blocks are discretized by a continuum mesh or "zones." Additionally, a deformable block can be assigned an elastic or inelastic constitutive model. Since UDEC does not allow block division once the model has been stepped, the use of inelastic zones within the blocks allows for the intragranular damage process to be approximated. Accordingly, the use of an inelastic constitutive model for the zones is important when modeling rocks under high confinement or in the postpeak portion of the stress-strain curve, where intragranular fracturing is prevalent (Abdelaziz et al., 2018; Peng et al., 2018). To represent the full range of rock behavior, a micromechanical model should therefore incorporate both elastic heterogeneity and zone inelasticity. To the authors' knowledge, only two studies applying this approach using Voronoi BBMs (Sinha & Walton, 2019, 2020) have been made to date. All other previous studies have used one of the three following representations: (a) homogeneous elastic (e.g., Ghazvinian et al., 2014; Stavrou & Murphy, 2018)—only one set of properties was assigned to all blocks and contacts and the zones were elastic, (b) homogeneous

inelastic (e.g., Noorani & Cai, 2015; Wang & Cai, 2019)—only one set of properties was assigned to all blocks and contacts, but the zones were inelastic, and (c) heterogeneous elastic (e.g., Chen & Konietzky, 2014; Lan et al., 2010; Park et al., 2017)—the properties were based on the mineral type, contact properties were assigned individually based on the mineral-mineral associations, and the zones were elastic. Accordingly, none of these studies were able to produce reasonable postpeak stress-strain behavior across a wide range of confining stresses; a detailed discussion on the advantages and disadvantages of each of the three model representations can be found in Sinha and Walton (2020). Even in studies that have employed zone inelasticity and block heterogeneity (Sinha & Walton, 2019, 2020), a close match to the postpeak shapes and the residual strengths for all levels of confinement considered could not be attained. These models were also not able to reproduce the CWFS strength behavior that is typically associated with brittle rocks.

Additionally, for the models that have been previously developed, no simple approach exists within UDEC to evaluate how grain-boundary crack growth and intragranular yield interact to influence strain field within the simulated specimens. UDEC has built-in functions for extracting strains, but these values correspond only to the block zones; consequently, the component of strain induced by block separation cannot easily be considered at the grain scale within the specimens. Although it is possible to extract the block separation magnitudes (i.e., displacements) using built-in UDEC functions, translating these into strain values is problematic and there is no well-established methodology for this purpose. The primary issue is that strain calculation requires a reference length, and this reference length should ideally be zero for two nodes on separate blocks that were previously in contact but have separated.

Based on the existing state of the art as described above, the following research gaps were identified: (1) No previous BBM has been able to closely match the postpeak strength drops and residual strengths of brittle rocks for multiple levels of confinement, (2) no previous BBM study has replicated macroscopic CWFS strength behavior, and (3) there is no existing methodology for quantifying the strains created due to block separation in UDEC. The motivation for this study is that if it can be established that BBMs are capable of reproducing the postpeak behavior (addressing research gaps 1 and 2), then it will be possible to gain more insight into the underlying damage mechanisms; this is critical given that it is very difficult to control this part of the stress-strain curve in actual compression tests (Diederichs, 1999, 2003). The use of such BBMs to study postpeak rock behavior will of course rely on the existence of analysis approaches (research gap 3) that allow for consideration of the interaction of block separation and zone yield, both of which are prevalent in the postpeak portion of the stress-strain curve (Abdelaziz et al., 2018; Sinha & Walton, 2020).

This study adopted a mobilized dilation angle model in the zones to address research gaps 1 and 2. This is in contrast to the models in Sinha and Walton (2020), which used a dilation model that linearly degraded the dilation angle from a peak to a residual value, independent of confining stress. Those BBMs were not able to fully reproduce the observed postpeak response or the expected CWFS behavior of Creighton Granite. In terms of analyzing the grain-scale strain field perturbations (research gap 3), a convenient methodology is to use 2-D digital image correlation (2-D-DIC), but its applicability to BBM (and more broadly to numerical models) is yet to be established. To that end, this study employs the 2-D-DIC approach in context of the UCS BBM to accomplish two primary goals: (1) quantify strains within the specimens, considering both crack and separation and zone strains (which is currently not possible with the built-in functions in UDEC), and (2) extend the 2-D-DIC approach from real rock testing to numerical models.

2. Rock Description and Model Setup

2.1. Description of Creighton Granite

The rock selected for this study is from the footwall of the Creighton mine in Sudbury, Canada (Walton, 2014). There is some variability in the mineralogical composition of the rocks across the footwall, but they are treated as a single geomechanical unit (termed as “Creighton Granite”; Walton, 2014). The rock has highly irregular mineral grains with an average size of 2.25 mm and is composed (on average) of approximately 55% Na-Feldspar, 30% quartz, and 15% biotite (Sinha & Walton, 2019). The average UCS and direct tensile strength for Creighton Granite are 203 and 9.0 MPa, respectively. The tensile strength was estimated from BTS data by applying a conversion factor of 0.86 (Perras & Diederichs, 2014). For the purposes of constraining the BBMs, triaxial data for 0–60 MPa confining stress (Walton, 2014), CI, CD, Young's modulus (E), Poisson's ratio (ν), and peak dilation angles were utilized (Table 1; Sinha & Walton, 2020; Walton, 2014).

Table 1
Geomechanical Properties of Creighton Granite

Property	Value
E (GPa)	69
ν	0.26
Peak strength (MPa)	$\sigma_3 + 181\left(\frac{\sigma_3}{8.66}+1\right)^{0.5}$; $m_i = 20.9$
CD (MPa)	$\sigma_3 + 133\left(\frac{\sigma_3}{16.4}+1\right)^{0.5}$; $m_i = 8.1$
CI (MPa)	$98 + 2.77\,\sigma_3$
β_0	1.1
β'	0.14

Note. Sinha and Walton (2020) and Walton (2014).
Abbreviations: CD: crack damage; CI: crack initiation.

The peak strengths and the CD thresholds were characterized using the Hoek-Brown formulation for intact rocks (Hoek et al., 2002), given by

$$\sigma_1 = \sigma_3 + \left[\sigma_{ci} \text{ or } \mathrm{CD}_{(\sigma_3=0)}\right]\left(m_i \frac{\sigma_3}{\left[\sigma_{ci} \text{ or } \mathrm{CD}_{(\sigma_3=0)}\right]} + 1\right)^{0.5} \quad (1)$$

where σ_1 and σ_3 are the major and minor principal stresses; σ_{ci} is the uniaxial compressive strength obtained by fitting equation (1) to uniaxial, triaxial, and tensile strength data; $\mathrm{CD}_{(\sigma_3=0)}$ is the CD threshold under unconfined conditions; and m_i is a fit parameter. Note that σ_{ci} and $\mathrm{CD}_{(\sigma_3=0)}$ might not be equal to the average UCS and average CD since they are obtained from a statistical fitting process that considers data other than those obtained under uniaxial loading conditions. Contrary to the nonlinear trend of peak strengths and CD thresholds, CI generally varies linearly as a function of confining stress.

2.2. Description of the Mobilized Dilation Angle Model

Volumetric changes in rock specimens under compression can be studied using the dilation angle (Ψ; Vermeer & De Borst, 1984). It has been found that the dilation angle in rocks varies both as a function of confining stress and plastic shear strain-plastic shear strain being a proxy for specimen damage (Alejano & Alonso, 2005; Walton & Diederichs, 2015a). A recently proposed mobilized dilation angle model, termed as the Walton-Diederichs (WD) model (Walton & Diederichs, 2015a), adjusts the dilation angle as a function of both confinement (σ_3) and plastic shear strain (ε_{ps}). The model formulation is presented in equations (2) and (3).

$$\Psi(\sigma_3, \varepsilon_{ps}) = \begin{cases} \dfrac{\alpha\,\varepsilon_{ps}\,\Psi_{\text{peak}}}{\varepsilon_{\text{m}}^{\text{ps}}\, e^{\left((\alpha-1)/\alpha\right)}} & \text{when } \varepsilon_{ps} < \varepsilon_{\text{m}}^{\text{ps}}\, e^{\left((\alpha-1)/\alpha\right)} \\ \Psi_{\text{peak}}\left(\alpha \ln\left(\dfrac{\varepsilon_{ps}}{\varepsilon_{\text{m}}^{\text{ps}}}\right)+1\right) & \text{when } \varepsilon_{\text{m}}^{\text{ps}}\, e^{\left((\alpha-1)/\alpha\right)} \le \varepsilon_{ps} < \varepsilon_{\text{m}}^{\text{ps}} \\ \Psi_{\text{peak}}\, e^{\left(-\left(\varepsilon_{ps}-\varepsilon_{\text{m}}^{\text{ps}}\right)/\varepsilon^{ps^*}\right)} & \text{when } \varepsilon_{ps} \ge \varepsilon_{\text{m}}^{\text{ps}} \end{cases} \quad (2)$$

$$\Psi_{\text{peak}}(\sigma_3). = \begin{cases} \varphi\left(1 - \dfrac{\beta'}{e^{-\left((1-\beta_0-\beta')/\beta'\right)}}\sigma_3\right) & \text{when } \sigma_3 < e^{-\left((1-\beta_0-\beta')/\beta'\right)} \\ \varphi\left(\beta_0 - \beta' \ln \sigma_3\right) & \text{when } \sigma_3 > e^{-\left((1-\beta_0-\beta')/\beta'\right)} \end{cases} \quad (3)$$

The WD model has five parameters (α, β_0, β', $\varepsilon_{\text{m}}^{\text{ps}}$, and ε^{ps^*}) and is characterized by an initial prepeak segment (defined by α), which increases up to a peak point (defined as a function of confinement by β_0, β', and $\varepsilon_{\text{m}}^{\text{ps}}$), and then decays following a negative exponential function (defined by ε^{ps^*}). The parameters β_0 and β' define the sensitivity of peak dilation angle to confinement, $\varepsilon_{\text{m}}^{\text{ps}}$ is equal to the plastic shear strain at which the peak dilation is achieved, α controls the curvature of the premobilization section of the dilation model, and ε^{ps^*} controls the rate of decay in dilation angle. For a particular rock, these parameters can be determined by fitting the mathematical model to uniaxial and triaxial laboratory compressions test data (Walton, 2014).

Walton et al. (2016) previously determined the WD parameters for Creighton Granite, and some of the relevant ones are listed in Table 1. The confinement-dependent dilation parameters that describe how the peak dilation angle varies as a function of confining stress (β_0 and β') are specifically reported here since they were chosen as calibration targets for the BBM. In other words, the BBM was calibrated to quantitatively exhibit

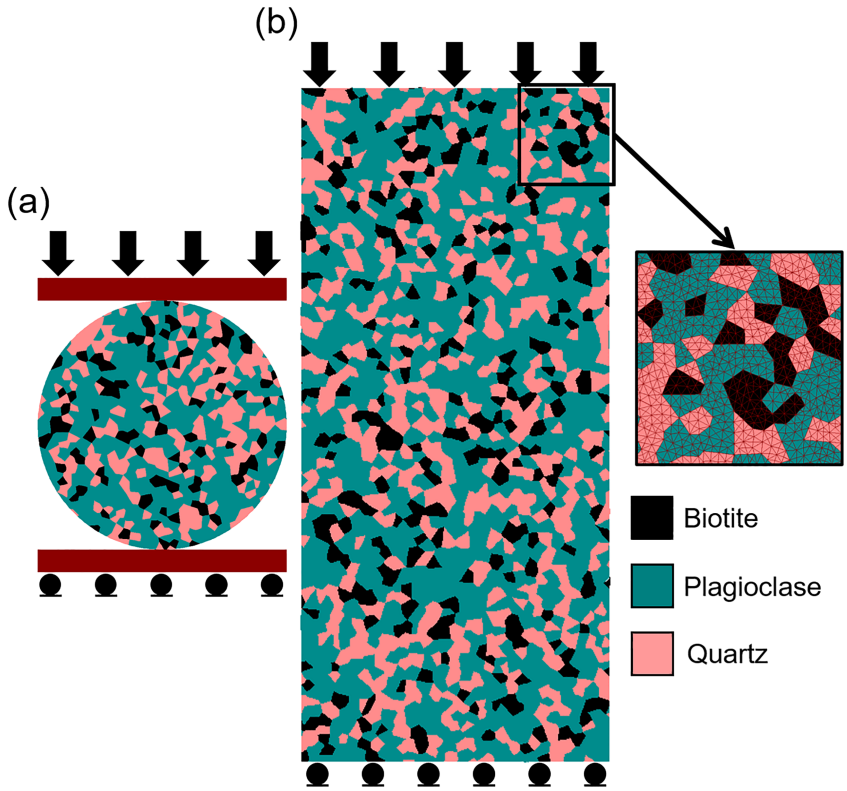

Figure 1. Bonded block model setup for (a) Brazilian tensile strength test and (b) UCS/triaxial test (after Sinha & Walton, 2020).

the confinement-dependent dilation phenomenon, which is the relative inability of a specimen to expand/dilate when confined.

2.3. Bonded Block Model Setup and Calibration

Numerical simulation of Creighton Granite was conducted using two separate model setups in UDEC-BTS and UCS/triaxial models (Figure 1). The BTS model was circular with a diameter of 55 mm, while the UCS/triaxial model was rectangular with a height and width of 120 and 55 mm, respectively. Two steel platens were positioned on either edge of the BTS specimen, and loading was conducted by restraining the bottom platen while allowing the top platen to move downward per a constant velocity. In the UCS/triaxial setup, no such platens were considered and the specimens were loaded directly via a constant velocity boundary along the model top. The lack of platens replicates an infinitely stiff loading system, which is justified in this case as the stress-strain curves for Creighton Granite from the laboratory had controlled post-peak behavior. For conducting the triaxial tests, a stress boundary was assigned to the lateral edges of the model. The velocities chosen for the BTS and UCS/triaxial models were 0.005 and 0.01 m/s, respectively, which are slow enough to mimic pseudo-static loading conditions (Fabjan et al., 2015; Kazerani & Zhao, 2010; Stavrou & Murphy, 2018).

Grain size distribution is known to have some effect on the macroscopic response of BBM, and it is accordingly ideal to map grain shapes and sizes using advanced image processing techniques and incorporate them into the modeled block structure (Li, Konietzky, & Frühwirt, 2017; Park et al., 2017; Tan et al., 2016). While such an approach has advantages in terms of model realism, in this particular case, we are attempting to model the behavior of rocks with a range of petrographic characteristics rather than a single specimen. Wang and Cai (2018) mention that where it is not possible/feasible to model the true grain size distribution, the average block size should at least be closer to the mean value. With that in mind, a 2 -mm block edge length and a small "iteration" value of 5 was input into the UDEC Voronoi generator to create a highly irregular block structure that had an average block size of 2.25 mm (Sinha & Walton, 2019). The iteration

parameter controls the irregularity of the block structure; a higher value corresponds to more regularity. The authors would like to point out here that irrespective of the iteration parameter value, elongated blocks conforming to the typical shape of biotite minerals could not be created. Therefore, the block structure in Figure 1 is only an approximation of the true grain morphology of Creighton Granite. Any disagreement between the actual grain geometries and the modeled grain geometries is implicitly accounted for in the material parameters obtained from model calibration. Once the model was constructed, the blocks were segregated randomly into three mineral groups, following the areal proportions as listed above. The elastic constants and density values were assigned separately for each of the mineral types based on the values recommended by Bass (1995) and Mavko et al. (2009).

To mimic the intragranular fracturing process, the Mohr-Coulomb strain-softening constitutive model was assigned to the zones within the different mineral blocks (Noorani & Cai, 2015; Wang & Cai, 2019). It would be most realistic to assign three different sets of strain-softening parameters to the three mineral types; as part of this study, we developed such a model, and it was found to be capable of capturing all the laboratory-derived attributes of Creighton Granite. However, models ran with a single set of inelastic parameters (derived by areal averaging the inelastic strength parameters for the three mineral grains) were also found to perform equally well in replicating the calibration targets. Since both models behaved similarly in reproducing the calibration targets, it was decided to employ the less complex homogenized inelastic zone property model for further analysis in this study. Note that it was only the inelastic strength parameters that were homogenized; the elastic constants and densities were assigned separately by mineral type.

The only refinement introduced in the strain-softening framework of UDEC is the representation of the dilation angle. Instead of a plastic shear-strain based dilation model, we considered the mobilized WD model (Walton & Diederichs, 2015a) in the zones. The motivation for the use of a mobilized dilation model is based on logical extrapolation—if a mechanism applies to a rock specimen, then it should apply to its constituents as well. This can also be justified on grounds that the mechanism by which a fracture is formed and its response to loading is not dependent on the scale of the problem. Whether at a microscale or a macroscale, with shearing (expressed via ε_{ps} in the WD model), the asperities on a newly developed fracture surface will degrade and dilatancy will reduce. On the other hand, if confinement is increased, then the ability of extensile fractures to open will be limited and this will manifest in a lower peak dilation angle.

When the WD dilation model is used in conjunction with a strain-softening constitutive model, the prepeak parameters are not required (Walton & Diederichs, 2015a). In other words, the entire dilation model can be defined by three parameters (β_0, β', and ε^{ps^*}). This is beneficial both from a calibration as well as a phenomenological standpoint. Three input parameters are required in the default plastic shear strain-based dilation model in UDEC, and so the choice of the WD mobilized dilation angle model does not increase the number of input parameters. Using only three parameters, both the plastic shear strain and confinement dependencies of dilation angle are still represented in the model zones. The WD parameters used in the BBM zones were chosen directly from Walton et al. (2016). While these were also varied as a part of the calibration process, the model results were found to not be especially sensitive to the dilation parameters over the range of values typical for most rocks and minerals; rather, the use of the mobilized model itself appeared to have a large impact in and of itself (relative to a simplified dilation model in UDEC).

The calibration methodology followed for determining the best fit parameter set has been discussed in the context of simpler models by Sinha and Walton (2020). In Sinha and Walton (2020), results corresponding to a heterogeneous, inelastic BBM were also presented, but that model utilized the built-in plastic shear strain-based dilation model instead of the mobilized dilation model. Various parametric combinations were tested, and it was found impossible to capture the postpeak behavior and the residual strengths of Creighton Granite with a basic plastic shear-strain-dependent dilation model. In particular, those models underpredicted the residual strengths at low confinement and overpredicted them at higher confinement. Such a finding can be explained based on that fact that a confinement-independent dilation model would tend to underestimate the grain dilatancy at low confinement and to overestimate it at higher confinement. Since higher dilation angles generate more local confining stresses, this leads to anomalously low model strengths at a given strain level under low confinements and anomalously high model strengths under high confinements. Of course, the influence of the specific dilation angle model used is only notably when there is a

Table 2
Zone Input Parameters for the Calibrated BBM

Cohesion (MPa)		Friction angle (deg)		Tensile strength (MPa)			WD model parameters		
Peak (c_{peak})	Residual (c_{res})	Peak (φ_{peak})	Residual (ϕ_{res})	Peak ($\sigma_{t,peak}$)	Residual ($\sigma_{t,res}$)	ε_{ps}	β_0	β'	ε^{ps*}
118.5	48.5	65	47.8	51.5	0	0.1	1.1	0.1394	0.01

Note. ε_{ps} is the plastic strain over which the parameters degraded from peak to residual values.
Abbreviations: BBM: bonded block model; WD: Walton-Diederichs.

significant amount of zone yield in the BBM (i.e., in the postpeak portion of the stress-strain curve and under triaxial conditions).

With all this in mind, we employed a model considering the complete strain-dependent dilation angle mobilization and decay process and confinement dependency to replicate the postpeak behavior and the residual strengths of Creighton Granite. The contribution of the dilation model only becomes significant when the zones start to yield within the model, and this was found to occur close to the CD threshold. It therefore follows that the behavior of the current BBMs is similar to those in Sinha and Walton (2020) up to the CD threshold. The calibrated zone parameters (strength and dilation model) and the block contact parameters are listed in Tables 2 and 3, respectively.

While other studies have attempted to identify mineral-specific parameters to simplify the calibration process for different rock types (Villeneuve, 2008; Villeneuve et al., 2009, 2012; Villeneuve & Siratovich, 2015), the strength parameters in this study (Table 2) were chosen purely on the basis of their ability to reproduce the different calibration targets. With that said, the stiffness properties for the minerals were not calibrated and were selected as "mineral-specific" inputs from Bass (1995) and Mavko et al. (2009). It should also be noted that the parameters in Table 2 were obtained specifically for Creighton Granite and as such might not be directly applicable to other rock types. To simulate other rock types, either the methodology outlined in Sinha and Walton (2020) could be followed or the parameters in Table 2 could be used as a starting point followed by iterative adjustments.

2.4. Methodologies for Analyzing the BBM Results

To track the evolution of stress, axial strain, and lateral strain, user-defined FISH functions were implemented in UDEC. In the UCS/triaxial models, axial stress was determined by dividing the sum of the reaction forces along the model top by the width of the specimen. Axial and lateral strains were determined by tracking each of the grid points along the shorter edges and 10 pairs of grid points along the longer edges of the model, respectively. In addition, the mode of fracture formation (i.e., tensile or shear) was also tracked for all contacts in the model. For the BTS model, the sum of reaction forces (P) along the top platen was converted to tensile stress using the equation: $\sigma_t = {}^{2P}/_{\pi Dt}$, where D is the diameter and t is the thickness of the model (unity for a 2-D model).

It is important to replicate the laboratory-obtained CI and CD thresholds in BBMs alongside peak strengths to ensure that the models are replicating the microdamage process accurately. The CI threshold is generally determined from laboratory data using the reversal point of crack volumetric strain or nonlinearity in the axial stress-lateral strain curve, while the CD threshold can be identified from the reversal of volumetric strain or the point of nonlinearity in the axial stress-axial strain curve (Diederichs, 2003; Diederichs & Martin, 2010; Martin & Chandler, 1994; Nicksiar & Martin, 2012). Crack volumetric strain ($\varepsilon_{v,\ crack}$) represents the inelastic portion of the total volumetric strain (ε_v) and is calculated using the following equation (Martin & Chandler, 1994):

$$\varepsilon_{v,\ crack} = \varepsilon_v - (\sigma_1 - \sigma_3)\frac{(1-2\nu)}{E} \quad (4)$$

The volumetric strain reversal approach has been found to overestimate the confined CD thresholds in crystalline rocks. Diederichs (2003)

Table 3
Contact Input Parameters for the Calibrated BBM

Contacts	$j\,kn$ (GPa/m) $\times 10^4$	j coh (MPa)	j fric (deg.)	j tens (MPa)
Q-Q	28	105	63	28
P-P	25	95	61	27
B-B	13	80	58	20
Q-P	23	90	53	21
Q-B	23	60	51	18
P-B	23	60	51	18

Note. Q: quartz; P: plagioclase; B: biotite.
Abbreviation: BBM: bonded block model.

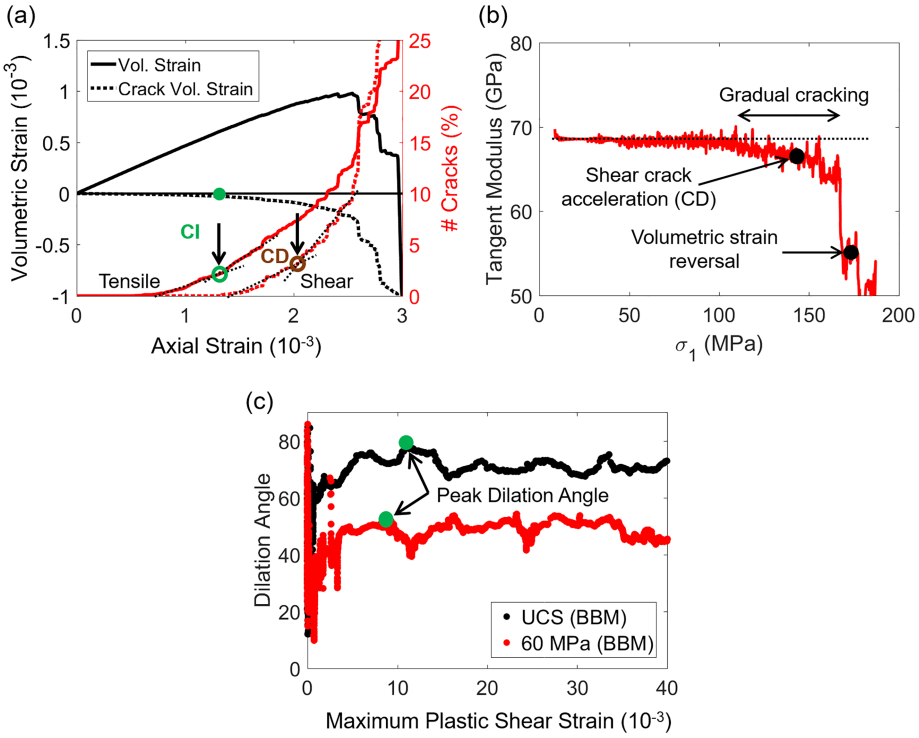

Figure 2. (a) Methodology for identifying crack initiation and crack damage (CD) as shown for UCS bonded block model (BBM) results, (b) Tangent modulus plot for UCS BBM indicating the discrepancy in the point of volumetric strain reversal and shear crack acceleration, and. (c) Identifying the peak dilation angle from dilation angle versus maximum plastic shear strain plots.

explained the cause of this discrepancy based on the simultaneous increase in the axial and lateral strain rate following the initial interaction of microcracks, which creates a lag in the onset of dilatancy. As a result, the point of axial stress-strain nonlinearity is the universal definition of the CD threshold (Diederichs & Martin, 2010).

In micromechanical models, it is more common to identify the CI and CD thresholds from the point of acceleration in the tensile and shear crack curves, respectively (Diederichs, 1999; Farahmand & Diederichs, 2015; Ghazvinian et al., 2014). The authors in a recent study developed an approach to determine these "acceleration points" from tensile and shear crack curves normalized to the total number of tensile and shear cracks in the models at the residual stress levels (Sinha & Walton, 2020). The points of first significant change in slope in the two normalized curves were chosen as the CI and CD, respectively (see Figure 2a). These points also corresponded well with the points of nonlinearity in the axial stress-lateral strain curve (CI) and the axial stress-axial strain curve (CD) from the BBMs. The match between the shear crack acceleration point and the point of nonlinearity in the axial stress-axial strain curve is illustrated using a moving average plot of tangent modulus values in Figure 2b. Tangent modulus is a measure of the slope of the axial stress-axial strain curve and the deviation from horizontal indicates inelastic deformation in the axial direction (i.e., the CD threshold).

During the course of model calibration, the authors observed a lag in the point of volumetric strain reversal and acceleration of the shear cracks in the UCS model (Figure 2a). The lag in the point of volumetric strain reversal and the axial stress-axial strain nonlinearity is concerning, as most of the previous Voronoi BBM studies have identified the unconfined CD by choosing a point on the shear crack curve that is coincident with the reversal of volumetric strain (Farahmand & Diederichs, 2015; Noorani & Cai, 2015; Wang & Cai, 2019). To further highlight this discrepancy in the context of the models run as a part of this study, the volumetric strain reversal point is shown on the tangent modulus plot in Figure 2b. As can be observed, the volumetric strain reversal occurs at a much later phase when the tangent modulus has dropped by almost 20%. More interestingly, in each of the cited studies (Farahmand & Diederichs, 2015; Noorani & Cai, 2015; Wang

& Cai, 2019), this lag can be clearly noted. Since this study attempts to replicate the CD thresholds for both unconfined and confined conditions, the shear crack approach was followed throughout. The crack approach is preferred in BBM studies for determining the CI and CD as it is reliable and easier to implement in practice. The appropriateness of the axial stress-axial strain approach (coincident with the acceleration point in the shear crack curve) in the context of BBMs is verified later using the DIC approach.

Lastly, to compare the volumetric changes in the specimen with those measured in the laboratory, a normalized peak dilation angle (peak dilation angle normalized against the peak dilation angle under unconfined conditions) was calculated for each BBM. There are two advantages of using the normalization approach: (1) It is mathematically more convenient to fit a curve to such data as it has to pass through (0, 1). (2) It is easier to understand how changes to the input parameters affect the shape and size of the mathematical model. The readers are referred to Rahjoo and Eberhardt (2016) for more discussion on this topic. Previous BBM studies have only qualitatively explored the confinement-dependent dilatancy phenomenon using volumetric strain-axial strain plots (Farahmand & Diederichs, 2015; Noorani & Cai, 2015). The use of normalized peak dilation angle instead allows for a simple yet quantitative comparison with the laboratory data.

The determination of peak dilation angle for a specimen requires calculation of two separate quantities: the instantaneous dilation angles and the maximum plastic shear strains (γ^p). The methodology for calculating these two quantities can be found in Walton and Diederichs (2015a) and is briefly summarized here:

1. The instantaneous dilation angle (ψ) was determined from the equation (Vermeer & De Borst, 1984):

$$\sin(\psi) = \frac{\dot{\epsilon}_1^p + 2\dot{\epsilon}_3^p}{2\dot{\epsilon}_3^p - \dot{\epsilon}_1^p} \tag{5}$$

where $\dot{\epsilon}_1^p$ and $\dot{\epsilon}_3^p$ are the maximum and minimum plastic strain increments, respectively.

2. The maximum plastic shear strain (γ^p) is also a proxy for specimen damage and is mathematically calculated as

$$\gamma^p = \epsilon_1^p - \epsilon_3^p \tag{6}$$

If the dilation angle is constant, the two plastic parameters γ^p and ε_{ps} can be related via a constant at any point during plastic deformation (Walton, 2014). The relationship is more complex if the dilation angle varies as a function of the plastic parameter, but generally speaking, a constant conversion factor is applied in practice (Alejano & Alonso, 2005).

3. To satisfy the condition of yield at CD, that is, $\gamma^p = 0$ (Chandler, 2013; Zhao & Cai, 2010), γ^p was shifted by the value of γ^p at the CD threshold (γ_{CD}^p). This is necessary as the onset of nonlinearity in the axial and lateral strains is generally not coincident in rocks (Eberhardt et al., 1998; Zhao & Cai, 2010).
4. There are two ways of computing ϵ_1^p and ϵ_3^p: conducting loading-unloading tests and using the irrecoverable strains at the end of the unloading cycles to approximate the plastic strains or using the theory of elasticity to subtract calculated elastic components from the total strain to give ϵ_1^p and ϵ_3^p, respectively (Walton & Diederichs, 2015a). In this study, the latter approach was used to compute the plastic strain components.
5. The increments of plastic strains were then obtained by subtracting the plastic strains at an earlier stage of loading to those from a later stage. The axial strain gap between the "initial" and "final" point for each increment was 0.1 millistrain.

An example of instantaneous dilation angle plotted as a function of maximum plastic shear strain for the UCS and $\sigma_3 = 60$ MPa BBM is shown in Figure 2c. The maximum value of dilation angle is the peak dilation angle for the specimen (marked by green circle in Figure 2c). Once the peak dilation angles were identified, it was relatively straightforward to determine the normalized peak dilation angles.

3. Calibrated BBM Results and Discussion

Figure 3a compares the model-predicted peak and residual strengths to those measured in laboratory, and Figure 3b shows the stress-strain curves for the UCS, σ_3 = 10, 20, 40, and 60 MPa BBMs. As can be seen,

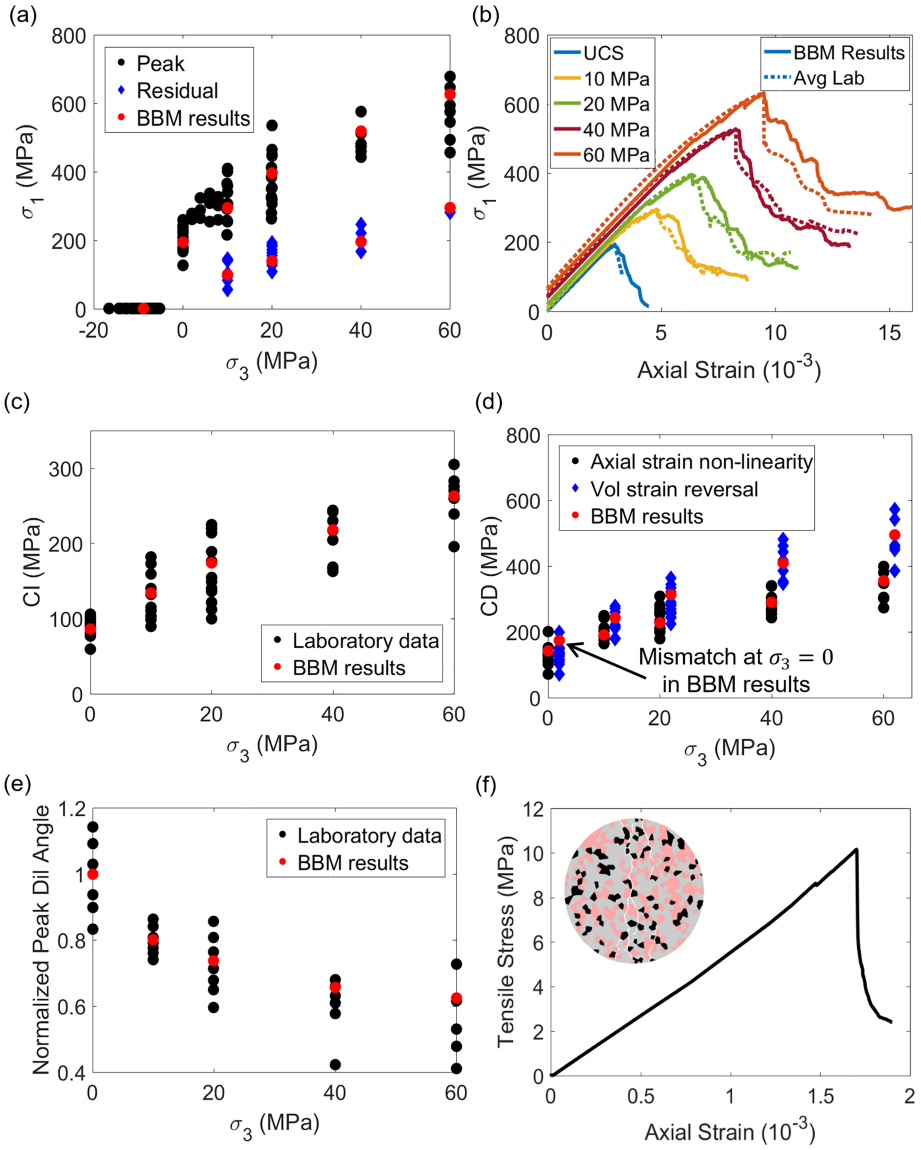

Figure 3. (a) Peak and residual strengths in σ_1-σ_3 space, (b) Average stress-strain curves for 0- to 60-MPa confinement, (c) CI thresholds (after (Sinha & Walton, 2020)), (d) crack damage thresholds, (e) normalized peak dilation angle versus confinement, and (f) BTS stress-strain curve with fracture pattern just beyond peak. Note that the crack damage values calculated using the volumetric strain reversal approach in (d) have been shifted to the right by 2 MPa for visualization purposes. The black and blue datapoints in (a) and (c)–(e) are derived from laboratory, while the red datapoints are from the bonded block models (BBMs). Panel (f) is from BBM.

the nonlinear shape of the peak strength envelope and the residual strengths are well captured by the models. To ascertain if the shape of the postpeak segments of the stress-strain curves were consistent with those of Creighton Granite, average postpeak segments were calculated from the raw laboratory stress-strain curves.

For this purpose, all stress-strain curves for a single level of confinement were first normalized such that the peaks coincided at (1, 1), the strain axis was divided into bins of 0.01 length, and vertical stresses in each bin were averaged; finally, the averaged curve was rescaled such that the peak point corresponded to the average peak strength and strain for that particular level of confinement. Figure 3b compares the laboratory post-peak behavior with those obtained from the BBMs. The reason why the stress-strain curves begin at different σ_1 values is because a hydrostatic stress equivalent to the confining stress level was initialized in the BBM before the models were stepped (or, equivalently, before deviatoric stresses were applied). Since the

hydrostatic loading phase was not considered in the models, the laboratory curves were truncated to start at the end of the hydrostatic loading phase as well.

A good match was obtained for all confinements barring only the $\sigma_3 = 60$ MPa model. The cause for the discrepancy can be attributed to the fact that there was only one stress-strain curve for $\sigma_3 = 60$ MPa that attained the residual stress level (see Figure 3a) and that specimen happened to have a quartz vein in it (potentially leading to a more brittle response; Turichshev & Hadjigeorgiou, 2017). The models were also able to replicate the CI thresholds for the entire range of confinement considered (Figure 3c). These results are similar to those in Sinha and Walton (2020), but are provided here for completeness.

Figure 3d shows the CD thresholds for Creighton Granite determined using the axial stress-axial strain nonlinearity approach and the points of volumetric strain reversal. The two values diverged with increasing confinement as is expected based on the findings of Diederichs (2003) and Diederichs et al. (2004). While the models were able to replicate the CD thresholds (obtained using the shear crack acceleration approach) and the volumetric strain reversal points fairly well, a mismatch was noted at $\sigma_3 = 0$ (unconfined conditions). In particular, the volumetric strain reversal occurred at $\sigma_1 = 171$ MPa, while the axial stress-axial strain nonlinearity occurred at $\sigma_1 = 141$ MPa in the BBM. Such a mismatch is not present at $\sigma_3 = 0$ in the laboratory data.

When rocks are loaded above the CD stress level, significant inelastic damage is induced in both the axial and lateral directions that results in irreversible volume change (Bieniawski, 1968; Lajtai, 1998). To better understand this phenomenon in terms of the numerical models, it is useful to revisit Figure 2c that shows the instantaneous dilation angle as a function of maximum plastic shear strain. A reduction in the peak dilation angle with confinement is perceptible, but the models fail to capture the subsequent decay in dilatancy. One would expect the decay to be minimal under low confining stresses, but increase with an increase in confinement (Arzúa & Alejano, 2013; Walton & Diederichs, 2015a; Zhao & Cai, 2010). This is because at low confinement, fractures open laterally and the associated dilation angles are high ($\dot{\varepsilon}_1^p \sim 0$ in equation (5) $\psi \sim 90^o$). When the system is sufficiently confined, tensile Mode I crack opening is impeded and shearing begins along the grain boundaries. With continued loading, the asperities on the grain boundaries and on the newly developed fracture surfaces are progressively damaged, which manifests as a decay in dilation angle. The fact that the BBMs do not register this decay (see Figure 2c) is related to the contacts being unable to simulate the destruction of asperities. How to incorporate asperities in a BBM, either implicitly or explicitly, remains an interesting research question for future studies.

Despite the inability of the model to replicate the dilation decay phenomenon, its ability to quantitatively replicate the confinement dependency of dilation angle (Figure 3e) represents a notable improvement over previous models that have only qualitatively demonstrated this phenomenon (Farahmand & Diederichs, 2015; Noorani & Cai, 2015).

The simulated Brazilian tensile test stress-strain curve corresponding to the best fit parameter set is shown in Figure 3f. The peak strength is 10.2 MPa, which is only 0.2 MPa lower than the average BTS of Creighton Granite. Such a small mismatch is considered acceptable given that the standard deviation in the laboratory measured BTS values was 3 MPa. The fracture pattern in the BTS BBM just past the peak stress is also shown in Figure 3f and is consistent with those observed in Creighton Granite specimens posttesting. To the best of the authors' knowledge, no previous BBM studies have calibrated their models to as many attributes as have been considered in this study.

3.1. Cohesion-Weakening-Frictional-Strengthening (CWFS) Behavior

In the last decade, Hajiabdolmajid et al. (2002) introduced the CWFS model to simulate the failure behavior of brittle rocks. The development of this strength model was motivated by the inability of the conventional yield criteria (e.g., Mohr-Coulomb and Hoek-Brown) to replicate the damage zones around tunnels in massive to sparcely fractured rockmasses. As shear yield criteria assume cohesional and frictional strength to mobilize simultaneously, it is unsurprising that such models were unable to replicate the brittle rock damage process (recall that cohesion degrades first followed by friction mobilization in brittle rocks).

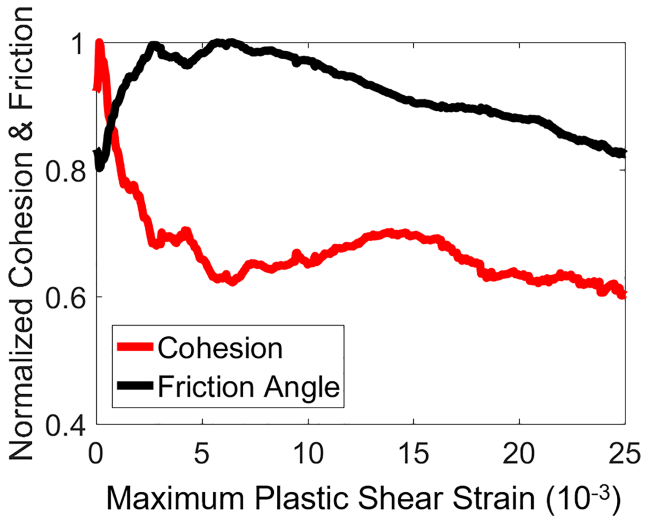

Figure 4. Cohesion and friction angle evolution with maximum plastic shear strain calculated at the specimen scale.

The CWFS model allows the cohesion to degrade and the friction angle to mobilize as a function of plastic shear strain. Since its introduction, the strength model has been successfully employed by numerous authors in reproducing notch formation around tunnels (Edelbro, 2009; Hajiabdolmajid et al., 2002; Zhao et al., 2010). More recently, Walton et al. (2016) used the CWFS model to numerically replicate the displacements measured by two multipoint extensometers in a pillar at Creighton mine. With the results of Walton et al. (2016) in mind, and noting the high ratio of UCS to tensile strength for Creighton Granite (22.7 in this case), the CWFS model can be expected to be applicable to Creighton Granite as well (Diederichs, 2007).

The cohesion and friction angle variation with maximum plastic shear strain were calculated for the calibrated BBM and are shown in Figure 4. To calculate these curves, axial stress versus maximum plastic shear strain curves were first developed for the unconfined and low confinement models ($\sigma_3 \leq 20$ MPa). Then, for different maximum plastic shear strains, straight lines were fitted to axial stress vs confinement plots using linear regression. The fit parameters in the σ_1- σ_3 space could then be converted into cohesion and friction angle using equations available in the literature (Hudson et al., 2002). During the course of this calculation, it was necessary to consider only the low confinement models to minimize the curvature in the strength data and to represent processes that are dominantly brittle (Walton, 2018).

As can be seen in Figure 4, the BBMs indeed exhibited a CWFS behavior in the initial stages of damage. To the authors' knowledge, this is the first time that a micromechanical model has been shown to capture the CWFS behavior. Postmobilization at ~6 millistrains, a continued decay occurred in the friction angle, while the cohesion (almost) leveled off and this is consistent with the findings of Martin and Chandler (1994). A similar behavior could not be obtained using the BBMs in Sinha and Walton (2020), likely due to of the improper representation of dilatancy in the zones. Zone dilation angle only influences the model behavior when there is a large amount of zone yield (i.e., under triaxial conditions and in the postpeak). As the CWFS calculation considers the postpeak model states for unconfined and triaxial simulations, it is understandable why the BBMs in Sinha and Walton (2020) were unable to produce such a behavior.

In any case, similar CWFS behavior has been observed previously from laboratory testing on conglomerate, Carrara marble, limestone, and Stanstead Granite (Walton, 2014, 2018; Walton & Diederichs, 2015b). Overall, the similarity in the trends of cohesion and friction angle to those in Martin and Chandler (1994) provides confidence in the ability of the BBM to replicate the strength characteristics of brittle rock.

3.2. Fracture Formation With Loading

The reliability of the BBM was further confirmed by comparing the fracture pattern in the models to trends reported in literature for similar rocks (Arzúa & Alejano, 2013; Tan et al., 2015). The model fracture patterns correspond to a stage when the respective residual stress levels were attained (Figure 5). Since these models possess intragranular fracturing capability via zone yield, all zones that were yielded and those zones which underwent significant inelastic shear during the loading process have also been highlighted in Figure 5 in blue and green, respectively.

The overall fracture mechanism transitioned from axial cracking to shear-banding as the confinement was increased from 0 to 60 MPa as is expected based on previous experimental studies on rocks (Arzúa & Alejano, 2013; Mair et al., 2002; Tan et al., 2015; Walton et al., 2017; Zhao & Cai, 2010). The inclination of the shear band (with respect to the horizontal direction) also decreased from ~77° in the $\sigma_3 = 20$ MPa BBM to ~63.5° in the $\sigma_3 = 60$ MPa BBM. A decrease in the shear band angle with confinement has been reported by Arzúa and Alejano (2013) and Paterson and Wong (2005). Vardoulakis (1980) provided a mathematical relationship between the orientation of the shear band (θ) and friction angle (φ) and dilation angle (ψ) for granular materials, given by

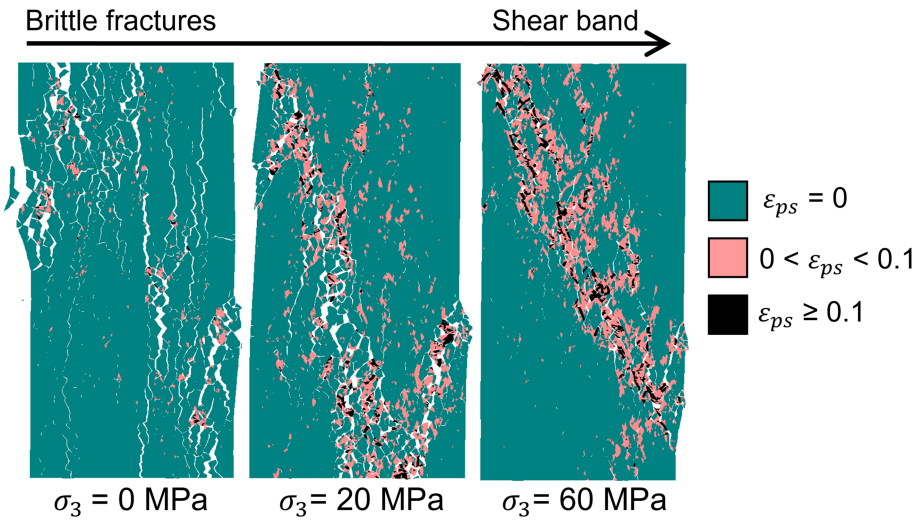

Figure 5. Fracture patterns in the UCS, 20 and 60 MPa models at their respective residual stress level.

$$\theta = 45^o + \frac{1}{4}(\varphi + \psi) \tag{7}$$

To obtain the instantaneous friction angles, a polynomial was first fitted to the BBM peak strengths for σ_3 = 0–60 MPa and then local derivatives were obtained at the confining stresses of interest. When this instantaneous friction angle and the instantaneous dilation angle at peak for the σ_3 = 20 MPa and σ_3 = 60 MPa were plugged into equation (7), θ values of 73 and 64° were obtained, respectively. The theoretical shear band angles are therefore within 5% of those observed in the BBM specimens.

Brittle UCS specimens often undergo axial splitting and are associated with large volumetric dilation. Some of these elongated fractures can be seen in the center and along the edges of the UCS model. There is only minimal zone damage, indicating that the failure occurs predominantly via grain-boundary fracturing. The extent of zone damage somewhat increases in the σ_3 = 20 MPa model, but elongated, axial fractures can still be observed (this justifies the use of $\sigma_3 \leq$ 20 MPa models in section 3.1). With further increase in confinement, a localized shear band develops across the specimen. Many more zones (with greater damage intensity) are involved in the ultimate failure, indicating the importance of intragranular fracturing under confined loading conditions.

Figure 5 only shows the final fracture patterns at residual stress levels but not the development of fractures with loading. To that end, plots of failed contacts at CD (141 MPa), the peak stress level (195 MPa), and 80% of the peak stress in the postpeak portion of the stress-strain curve (156 MPa) were extracted from the UCS BBM and are shown in Figure 6. At CD, some of the failed contacts interacted to form fractures about 2–4 mm long (1–2 block edge lengths). Increases in crack density with loading eventually resulted in the creation of elongated macrofractures aligned roughly along the direction of the minimum principal stress ("Peak" in Figure 6). As the specimen was loaded further postpeak, the macrofractures started to open, resulting in large volumetric dilation along the top left and bottom right corners of the specimen (blue lines in Figure 6). A similar behavior was noted in the confined BBMs with the only difference being the lower bulking in the specimens.

3.3. Fracture Orientation

Geometrical attributes of microcracks can provide more insight into the progressive damage development in the BBMs. To that end, orientations of the microcracks in the UCS specimen were determined at σ_1 = 141 MPa (CD), σ_1 = 175 MPa (volumetric strain reversal), and σ_1 = 195 MPa (Peak; see Figure 7a). These orientations are defined with respect to the horizontal direction and range from 0 to 180° (inset of Figure 7a). While interpreting Figures 7a–7c, it should be noted that the tops of the blue bars correspond to the sums of all the cracks. In the initial phases of loading (up to CD), most of the cracks were oriented

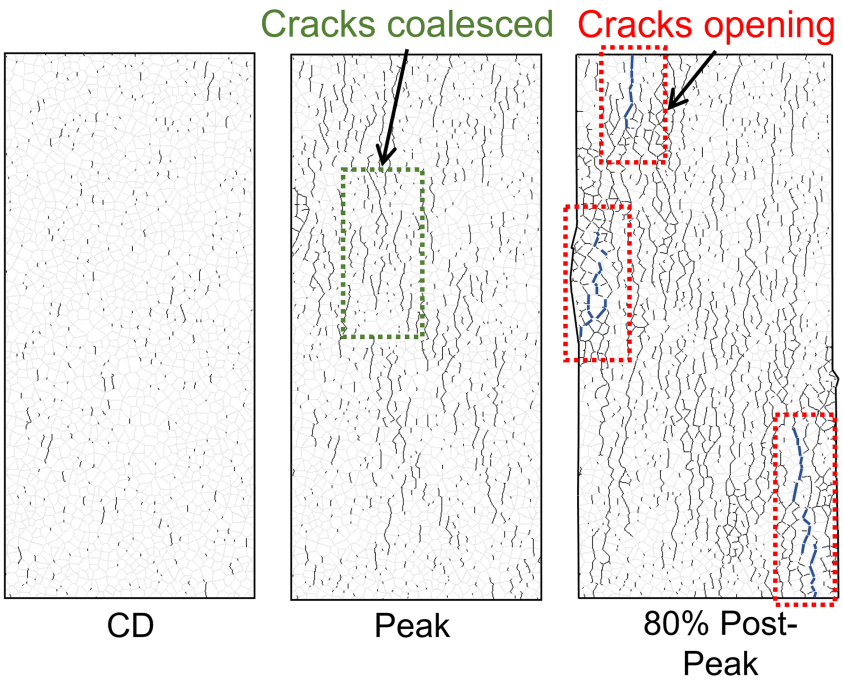

Figure 6. Crack evolution in the bonded block model at different stress levels.

parallel or subparallel to the major principal stress direction (60–120°). The crack generation process begins when the lateral strain generated by the Poisson effect exceeds a critical value. At a local scale, the lateral strain creates extensile normal stresses on the block contacts and the contacts rupture when the stresses exceed the respective tensile strength. Since the strains are generated normal to the longitudinal axis of the specimen, subvertical microcracks are naturally expected (also recall that cracking is primarily extensile in nature up to CD; Figure 2a).

As the applied load exceeds the CD, shear cracks develop within the specimen (Farahmand & Diederichs, 2015; Park et al., 2017). These cracks are generally inclined to the vertical direction, and this leads to widening of the orientation distribution. A similar behavior can be observed in the models of Park et al. (2017). It also seems that the orientation data follow a Gaussian distribution (mean at 90°) for all load levels.

The predominance of axially oriented microcracks in the early phases of loading has been previously reported by Paterson and Wong (2005) on the basis of optical observations on granite, with some cracks inclined up to ±35°. These cracks are generally confined to the boundaries of mineral grains and are extensile in nature (Eberhardt et al., 1999; Lee et al., 2006; Peng & Johnson, 1972; Tapponnier & Brace, 1976). As the loading is continued up to the peak, the proportion of the highly inclined cracks increases in reality (Wawersik & Brace, 1971; Wulff et al., 1999), similar to what is observed in the BBM (Figure 7a).

In the confined BBMs, although tensile cracks initiate first (Sinha & Walton, 2020), the number of shear cracks eventually exceeds the number of tensile grain-boundary cracks. Accordingly, the orientation distribution has its peak near 90° at the CD threshold (inset of Figure 7b) but flattens out (or even becomes slightly bimodal) between 50 and 130° at the peak strength. The crack geometries in Figure 7b correspond to the $\sigma_3 = 60$ MPa BBM at average axial stress levels of $\sigma_1 = 373$ MPa (CD), $\sigma_1 = 495$ MPa (volumetric strain reversal), and $\sigma_1 = 626$ MPa (Peak). To further analyze why the distribution did not resemble a Gaussian distribution, the shear and tensile crack orientations were plotted separately for the $\sigma_3 = 60$ MPa case when the model had reached its residual stress level (Figure 7c). It can be seen in Figure 7c that the flattening of the distribution is a compound effect of the bimodal nature of the shear crack orientation distribution and Gaussian nature of the tensile crack orientation distribution.

The bimodal nature of the shear cracks can be explained on grounds that the 90° plane corresponds to a plane of zero shear strain on a Mohr's circle (for the overall specimen stress state), and the frictional

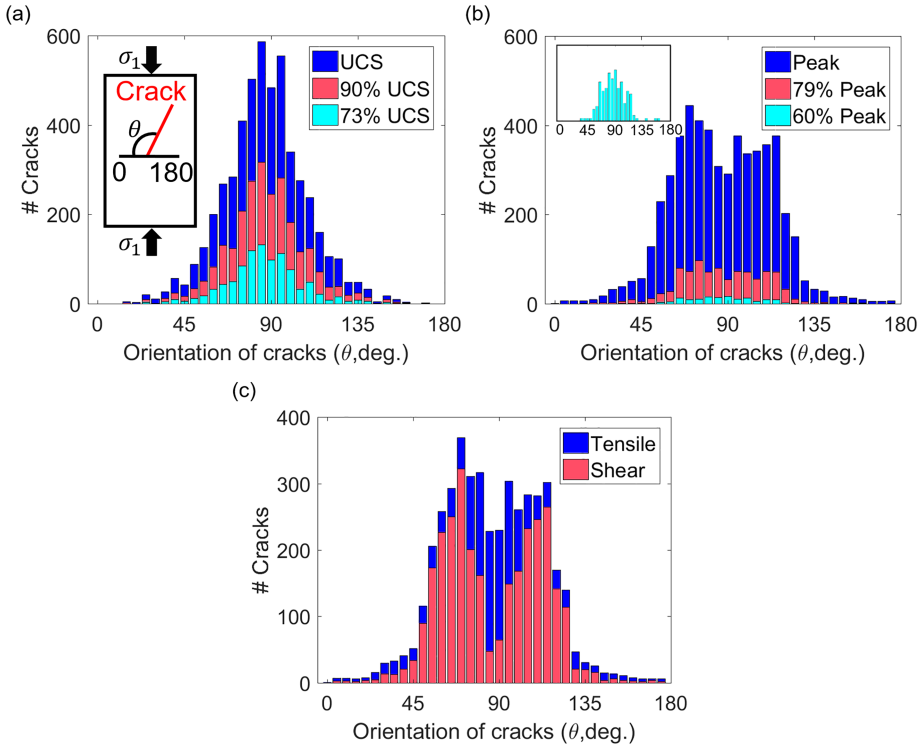

Figure 7. (a) Orientation of cracks at three different average axial stress levels in the UCS bonded block model (BBM). (b) Orientation of cracks at three different average axial stress levels in the $\sigma_3 = 60$ MPa BBM. The crack distribution at $\sigma_1 = 60\%$ Peak is enlarged in the inset. (c) Orientation of shear and tensile cracks in the $\sigma_3 = 60$ MPa BBM at the residual stress level. The tops of the blue bars in a–c correspond to the sum of the number of cracks.

forces on less inclined contacts are influenced more by the vertical stress rather than the lateral stress. The two peaks located ±20° away from the vertical are therefore the preferential conjugate orientations for shear crack development. This is supported by the observations of Wawersik and Brace (1971), who found the crack population oriented at ≥ ±20° to the vertical to increase in rocks tested under high confining stresses. These inclined microcracks eventually develop into a macroscopic shear fracture by linking up the en echelon inclined cracks (Paterson & Wong, 2005). Note here the similarity in the orientation of the macroscopic shear band as predicted by equation (7) (Vardoulakis, 1980) for $\sigma_3 = 60$ MPa (±26° to vertical) and the peaks of the shear crack count in Figure 7c. The other confined BBMs exhibited similar behavior, and the corresponding results are therefore not presented.

4. Investigating the Damage Localization in UCS BBM Using Two-Dimensional Digital Image Correlation (2-D-DIC)

The 2-D-DIC technique has found increasing use in recent years for studying the stress-induced fracturing process in rocks (Li, Zhu, et al., 2017; Shirole et al., 2019; Xing et al., 2018; Zhou et al., 2018). It is a robust, nondestructive, noncontact optical technique via which the full-field displacement and strain fields across a specimen surface can be monitored in real time (Pan et al., 2009; Sutton et al., 2009). Although most of the previous applications of 2-D-DIC pertain to physical laboratory tests on natural and man-made materials, an attempt has been made here to extend its applicability to numerical models, with the specific objective of capturing the effects of block separation on the effective strains in the simulated rock material. The UCS BBM is chosen for this purpose since failure in the UCS model is dominated by block separation (refer Figure 5) and this is the component of strain that is difficult to estimate using the functions available within UDEC.

4.1. Background of 2-D-DIC

The theory of 2-D-DIC has been reviewed in detail by numerous authors (e.g., Chu et al., 1985; Pan et al., 2009; Sutton et al., 2009), and accordingly, only a brief overview of the technique is presented here. The

2-D-DIC determines in-plane displacement and strain fields by tracking different regions or subsets on a specimen surface (in form of digital images) as it deforms progressively during the loading process. Typically, a random speckle pattern of gray-scale values serves as the carrier of the deformation information of the specimen surface (Pan et al., 2009; Schwartz et al., 2013). The idea is to identify the location of a subset in the deformed state with respect to its location in the reference (or undeformed) image. Each subset is composed of a number of pixels with different gray-scale values; the stochastic nature of the gray patterns helps in distinctly identifying the location of the subset in the different images (Hedayat et al., 2014; Pan et al., 2009).

The similarity of a subset in the deformed image and in the reference image is evaluated by correlation and cross-correlation criteria (Pan et al., 2009; Sutton et al., 2009). The position of the peak of the correlation coefficient distribution defines the position of a particular subset in the deformed image, and thereby the displacement of the subset. This calculated displacement is assigned to the center of the subset. Similarly, the displacements at the center of other subsets are calculated to obtain the full-field displacement across the surface of the specimen. Once the displacement field is calculated, the strain field can be determined following the pointwise local least squares technique of Pan et al. (2007, 2009). Pan et al. (2009) discussed how a numerical differentiation of the raw displacements might yield unreliable strains due to amplification of the noise in the displacement field. Accordingly, a smoothing approach (like the local least squares technique described below) is necessary before the strains can be estimated.

In the local least squares technique, a calculation window is first defined around a subset center for which the strain is to be calculated. A linear plane is then fitted to the local displacement field in this window following the least squares technique. The coefficients of the equations then allow for the determination of the Green-Lagrange strain tensor (E^*) and thereby the principal strains across the specimen surface. The out-of-plane components are ignored when calculating the principal strains from the normal (ε_{xx}, ε_{yy}) and shear strain (ε_{xy}) components (see equations (8)–(10)) of E^* (Chu et al., 1985; Tung et al., 2008):

$$\varepsilon_{xx} = \frac{\partial u}{\partial x} + \frac{1}{2}\left[\left(\frac{\partial u}{\partial x}\right)^2 + \left(\frac{\partial v}{\partial x}\right)^2\right] \tag{8}$$

$$\varepsilon_{yy} = \frac{\partial v}{\partial y} + \frac{1}{2}\left[\left(\frac{\partial u}{\partial y}\right)^2 + \left(\frac{\partial v}{\partial y}\right)^2\right] \tag{9}$$

$$\varepsilon_{xy} = \frac{1}{2}\left(\frac{\partial u}{\partial y} + \frac{\partial v}{\partial x}\right) + \frac{1}{2}\left[\frac{\partial u}{\partial x}\frac{\partial u}{\partial y} + \frac{\partial v}{\partial x}\frac{\partial v}{\partial y}\right] \tag{10}$$

where u and v are the displacement fields along the x and y directions, respectively.

4.2. 2-D-DIC Setup in BBM and Validation

A successful 2-D-DIC analysis requires the fulfillment of four important requirements: (1) A random speckle pattern is needed across the surface of the specimen, (2) the speckle size should be small and the gray-scale intensity values should have a relatively well-distributed histogram (Lin & Labuz, 2013), (3) the axis of the camera used for capturing the images must be parallel to the surface normal of the specimen, and (4) the camera should be placed sufficient far away such that the error in displacement measurements due to out-of-plane deformations is minimal (Pan et al., 2009). The last two requirements are automatically met in this study as the images for DIC analysis were extracted from a numerical model (no camera) and there is no out-of-plane deformation owing to the plane-strain formulation of UDEC.

To develop the artificial speckle pattern for the UCS BBM, the following steps were followed:

1. The addresses of each grid point (grid points are the vertices of the triangular zones) in the undeformed or unrun model were extracted. Across a block contact, UDEC usually duplicates a grid point such that each of the grid points are affiliated to one of the blocks in contact (refer to the red circle in Figure 8a). This is necessary so as to permit failure and separation along the contacts (Itasca, 2014).
2. From the list of grid point addresses and their coordinate locations, all duplicate grid points were identified and removed (Figure 8a). This step is vital to be able to incorporate the strains induced by the explicit opening of cracks. When two blocks start to detach in the BBM, additional deformation will be induced in the zones across the separating contact since one of the duplicate grid points has been removed. By

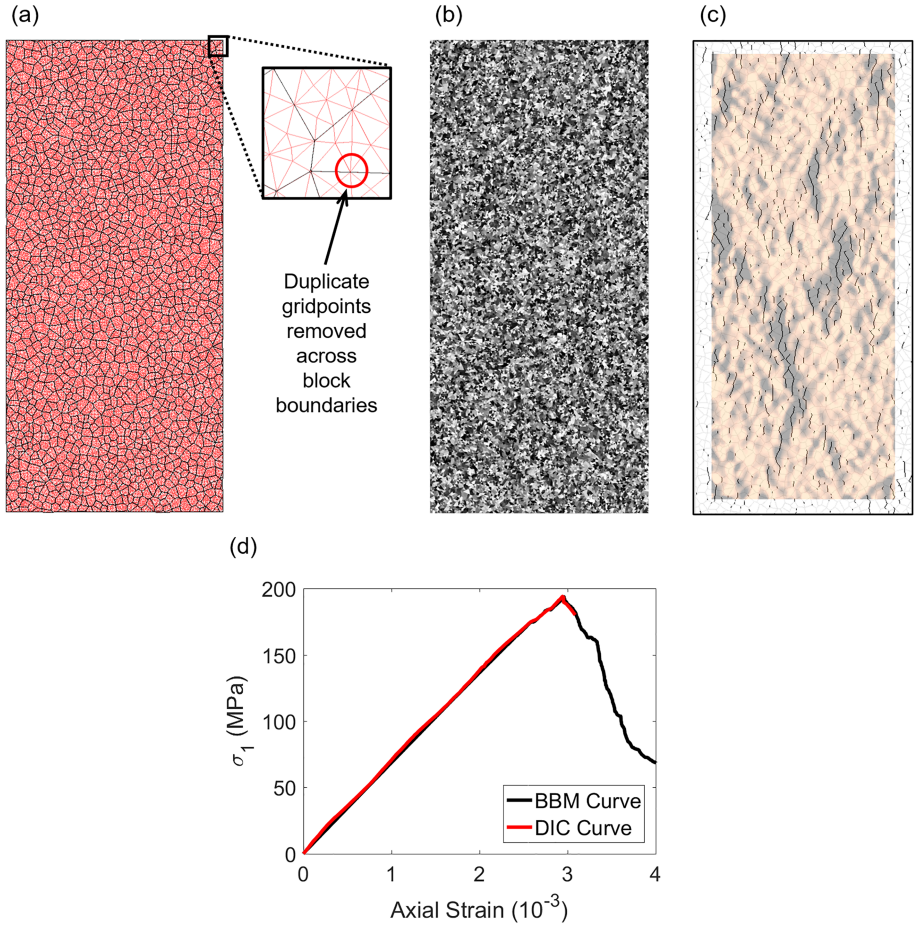

Figure 8. (a and b) Methodology followed for generating an artificial speckle pattern from the bonded block model (BBM). (c) Failed contacts from BBM overlaid on the digital image correlation (DIC) strain image at peak strength. (d) Comparison of the axial stress-axial strain curves from BBM and DIC analysis.

tracking the vertices of all the zones, the strains due to both inelastic damage and block separation can be accounted for in the analysis. It is important to note that this step is performed as a postprocessing step (i.e., the duplicate grid points are not removed in the BBM models but from the list of grid points that are tracked during the simulation). In context of the UCS BBM, the contribution of zone damage toward the strain field perturbations can be expected to be minimal (refer Figure 5).

3. The coordinates of all the grid points in the final list were extracted from UDEC once every 5,000 solution steps and were subsequently imported in MATLAB. Using a combination of Delaunay triangulation and surface plots, the triangular zones were reconstructed and colored randomly per a uniform distribution (Figure 8b). For all subsequent deformed images, it was ensured that the same color value was assigned to a particular speckle (analogous to the assumption that a speckle does not change color during the damage process). The use of a uniform distribution for coloring the triangular speckles fulfills the well-distributed histogram requirement of DIC analysis. As for the size of the speckles, zones are the smallest elements in a BBM, and obtaining a speckle smaller than the zone size is not possible. The accuracy of the computed strain and displacement fields could be possibly enhanced by reducing the zone size, but only at the expense of longer simulation time.

It might seem intuitive to conduct the DIC analysis without step "2" (i.e., with explicit fractures in the image) as is done for real rock tests, but there are specific issues with employing this approach. First, if the images are extracted directly from UDEC, the line thickness in block geometry plots tends to lead to an underestimation of the strains due to block separation. Secondly, if the images are reconstructed in MATLAB, as was done in this case, it is not possible to create Delaunay triangles with intermittent white spaces (i.e., explicit fractures).

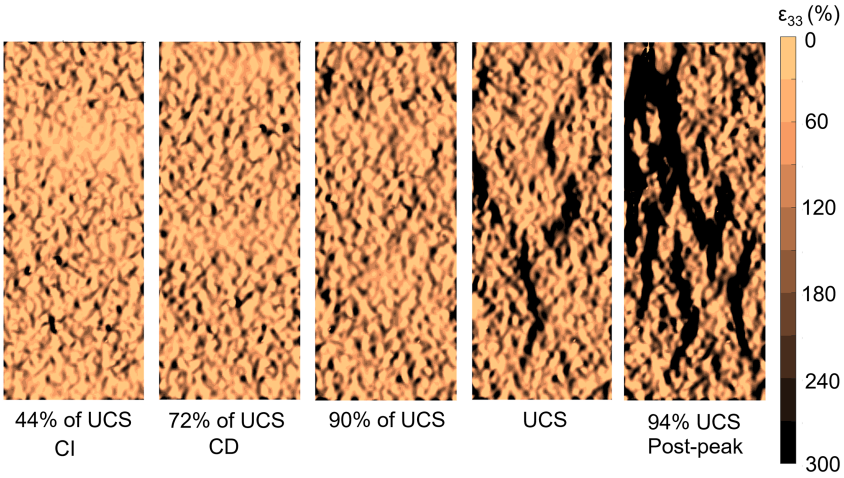

Figure 9. Strain fields in the UCS bonded block model for different stress levels obtained from the digital image correlation analysis.

Once the artificially speckled images for the undeformed and deformed model geometry were generated, it was subsequently analyzed in VIC-2D software. Subset and step sizes of 15 pixels and 5 pixels, respectively, were chosen for analysis. The step size defines how far apart the center of the neighboring subsets is located, and typically, it is selected to be smaller than half the subset size (Hedayat et al., 2014; Patel & Martin, 2018). A step size of 5 ensured that the neighboring subsets overlapped with each other, which leads to added accuracy in the estimated displacement field (Hedayat et al., 2014).

The reliability of the 2-D-DIC analysis was evaluated first by comparing the fracture pattern in the UCS BBM at peak strength to the regions of strain localization from the DIC analysis. From Figure 8c, it can be seen that the high strain regions (red) coincide well with the failed contact locations in the BBM. The DIC analysis was not extended all the way to the boundary of the specimen due to issues with selection of the strain calculation window; along the edges of an image, there are fewer pixels in the strain calculation windows and this leads to substantial noise in the estimated strain field. As a method validation, the full-field axial strains were averaged at each stress level across the specimen surface and compared to the axial strains measured from the numerical model. The two curves match well up to slightly beyond the peak strength (Figure 8d), and this establishes the applicability of 2-D-DIC to numerical modeling results.

DIC analyses are not suited for analyzing large deformations, and consequently, model states in the postpeak regime were not examined in great detail. In particular, the basic DIC assumption of preserving the speckle pattern during the deformation process is violated (Bourcier et al., 2013) and the correlation/cross-correlation methodology for mapping the subsets across the different images starts to fail.

4.3. 2-D-DIC Analysis: Results and Discussion

Figure 9 shows the minor principal strain (ε_{33}) for the UCS BBM at five different stress levels, normalized to the average specimen-scale lateral strain at peak strength (-1.31×10^{-3}; the negative value indicates extensional strain). The minor principal strain values are more sensitive to the microcracking process than the other strain directions and were therefore employed for further analysis (Shirole et al., 2019). As can be seen, at low levels of axial stress (44% UCS), the strain field is somewhat nonuniform, and this is attributed primarily to the elastic mismatch between the mineral blocks, as the amount of microcracking in the specimen prior to the CI threshold should be limited (Eberhardt et al., 1998; Lan et al., 2010). At an axial stress equal to 90% of the UCS, the strain concentration distinctly increases and forms subvertical bands. The elongated strain patterns signify the formation of extensile microcracks along the longitudinal axis of the specimen, and this is known to be the dominant mode of damage development in brittle rocks (Ghazvinian, 2015; Lan et al., 2010; Walton, 2014). The predominance of tensile cracks in the BBM at this loading stage also supports this reasoning (Sinha & Walton, 2020). The extent of strain localization can be further appreciated from the fact that at a load corresponding to 90% of the UCS, the local strains are >300% of the specimen-scale

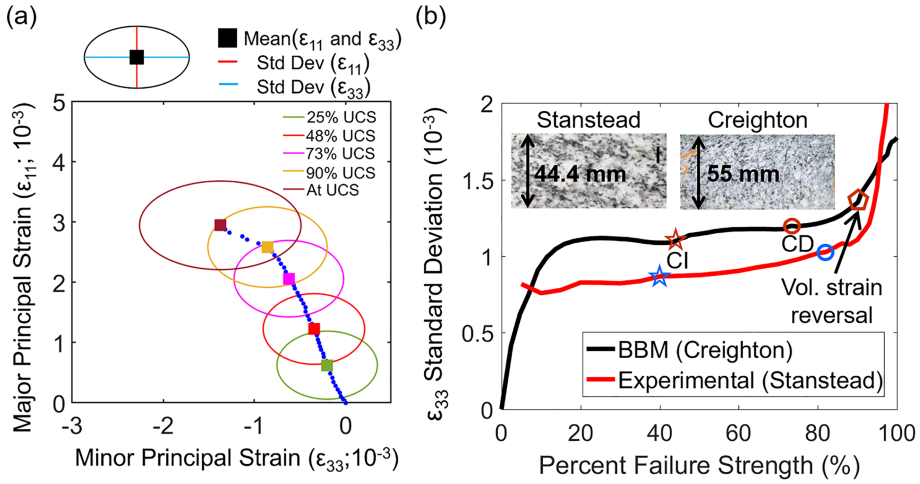

Figure 10. (a) Strain ellipses for five different load levels. (b) Comparison of the standard deviation of minimum principal strains in the bonded block model (BBM) and for Stanstead granite (Shirole et al., 2020) as a function of percentage failure strength.

lateral strain at the peak load. As the sample was loaded to its UCS and beyond, damage zones were clearly perceptible, and these regions coincided with the failed contacts in the BBM (see Figure 8d). Overall, the results indicate that the DIC analysis was successful in capturing the progressive damage formation in the model.

Diederichs (1999) and Lan et al. (2010) previously demonstrated using micromechanical models how the heterogeneity in the stress fields increases with increase in specimen damage. The study by Diederichs (1999) was performed using an early version of Itasca's Particle Flow Code, while Lan et al. (2010) used an elastic heterogeneous BBM. Lan et al. (2010) further related the variations in the axial stress field with the CI and CD observed in their models. With the full-field strains computed for the UCS BBM, it was possible to visualize this heterogeneity in terms of strains rather than stresses at different load levels. Figure 10a shows the strain ellipses at σ_1 = 25% UCS, σ_1 = 44% UCS (CI), σ_1 = 73% UCS, σ_1 = 90% UCS (CD), and σ_1 = UCS load levels as obtained from the 2-D-DIC analysis. The length of the major and minor axes of the ellipses correspond to the standard deviation of the minor (ε_{33}) and major (ε_{11}) principal strains, respectively, and signifies the heterogeneity in the strain fields.

Prior to occurrence of any microdamage (below 44% UCS; CI), some heterogeneity can be observed in both the major and minor principal strain fields. This is attributed to the multiminerallic nature of the model, where the different mineral blocks deformed in a dissimilar fashion depending on the local stresses and elastic modulus. Shirole et al. (2020) also reported a more homogeneous strain field in Lyon sandstone (composed of quartz grains with some clay cement) in comparison to Stanstead and Barre Granites (multiminerallic). With increasing load levels, the ellipses became larger and indicate an increase in heterogeneity with progressive damage. An interesting thing to note here is that the standard deviation of the minor principal strain field is always larger than that of the major principal strain field, and the ellipses become more elongated at greater load levels (i.e., after more damage has been induced). This implies that the minor principal strain field is more sensitive to the microcracking process, which is somewhat intuitive as the cracking in the UCS model is dominantly along the specimen axis (refer to Figure 7a).

Taking advantage of this fact and utilizing some laboratory test results on Stanstead Granite specimens (Shirole et al., 2020), a comparison of the ε_{33} standard deviation values (as a proxy for damage) were made to ascertain if the strain field perturbations in the BBM were realistic. This comparison is unique in the sense that it relates to local strains rather than stresses, which can be directly measured during laboratory compression tests (using strain gauges or DIC). The geomechanical parameters and petrological characteristics of Stanstead Granite are different than those of Creighton Granite, and therefore, a quantitative comparison would not be appropriate. With that in mind but recalling that both rocks are roughly granitic in composition, it can be expected that the overall trends and magnitudes of ε_{33} standard deviation will at least be

similar. The average UCS and modulus of Stanstead Granite is 129 MPa and 44 GPa (Shirole et al., 2020), while the mineralogical composition is approximately 25% quartz, 65% feldspar, and 9% biotite (Nasseri & Mohanty, 2008). The mean (volume averaged) grain size is 1.34 mm (Nasseri & Mohanty, 2008), which is smaller than that of Creighton Granite. For more details on Stanstead Granite testing and associated 2-D-DIC analysis, readers are referred to Shirole et al. (2020).

Figure 10b shows representative photos of Stanstead Granite and Creighton Granite specimens. Note the similarity in the mineralogical compositions of the two rock types. Since the UCS values of the two rock types are different, it was necessary to plot the standard deviations as a function of normalized failure strength so as to be able to compare the overall trends in the values. CI and CD for Stanstead Granite were computed using the reversal of crack volumetric strain and axial stress-axial strain nonlinearity approach, respectively (Shirole et al., 2020). The axial and lateral strains were determined through averaging the ε_{yy} (vertical) and ε_{xx} (horizontal) strain fields across the entire surface of the specimen. For Stanstead Granite, the point of axial stress-axial strain nonlinearity (i.e., the CD threshold) was found to coincide with the volumetric strain reversal point, as has been observed for other crystalline rocks.

With regard to the standard deviation curves, the following observations can be readily made:

1. The overall trend and the magnitudes of the ε_{33} standard deviation in the Creighton Granite UCS BBM are very close to those of Stanstead Granite.
2. The CD values for Stanstead Granite and Creighton Granite are located similar distances for their respective points of acceleration in the standard deviation curves. This serves as a secondary confirmation that the axial stress-axial strain nonlinearity or the shear crack approach yields a reliable CD value for the BBM under unconfined conditions.
3. The point of volumetric strain reversal corresponds to a model state that has experienced more damage than is typically expected in real rocks at CD.

A major point of concern in relation to the last observation is that many previous BBM studies (Farahmand & Diederichs, 2015; Noorani & Cai, 2015; Wang & Cai, 2019) have used the stress at volumetric strain reversal to determine CD under unconfined conditions. It is therefore likely that the CD was overestimated and the microproperties obtained from model calibration may be slightly off. The exact cause for the mismatch between the volumetric strain reversal point and axial stress-axial strain nonlinearity point in UCS-BBM is not well understood and should be studied further. In any case, it is recommended that future studies employing block models should use the axial stress-axial strain nonlinearity point or "acceleration" of shear cracking (as discussed in section 2) for identification of the CD threshold.

5. Conclusions

BBM are a useful tool for studying the microfracturing process in rocks. The model input parameters are generally constrained by comparing the macroscopic behavior of the models to those observed from laboratory testing. Conventional calibrations are restricted mostly to pre-peak attributes, like Young's Modulus, Poisson's ratio, unconfined CI, unconfined CD, tensile strength, and low confinement peak strengths. In this study, a multiminerallic BBM with inelastic zones has been developed, and it was shown to not only match the commonly considered calibration targets but also the confined CD, postpeak behavior (including residual strength), high-confinement strengths, and the decrease in peak dilation angle as a function of confinement for a granitic rock (Creighton Granite). To replicate the postpeak stress-strain behavior, residual strength, and dilation angle, it was necessary to use a mobilized (confinement and plastic shear strain dependent) dilation angle model for the model blocks.

As a methodological advancement and to improve our understanding of how strain heterogeneity evolves in block models, a 2-D-DIC analysis was conducted on the UCS model results. It was found that the minor principal strains (ε_{33}) are more sensitive to the microcracking process than the major principal strains (ε_{11}). Given the greater sensitivity to damage development, standard deviations of ε_{33} at different load levels were computed and compared to those for a different granitic rock for which laboratory test data including DIC results were available. A close correspondence in the overall trend was observed. With the methodology established for UCS BBM, future studies can apply it to confined BBMs as well to obtain strains due to both block separation and zone yield.

Lastly, the ε_{33} standard deviation values were utilized to examine the discrepancy in the point of volumetric strain reversal and the axial stress-axial strain nonlinearity in the unconfined BBM. Using the 2-D-DIC results, it was confirmed that the axial stress-axial strain nonlinearity is indeed the more appropriate indicator of CD in the unconfined BBM, and the volumetric strain reversal point corresponds to a slightly advanced damage state. The close correspondence of the 2-D-DIC analysis results and the ability of the model to match prepeak and postpeak attributes highlights the phenomenological capabilities of the calibrated BBM and more generally the BBM approach.

Acknowledgments
The research conducted for this study was funded by the National Institute for Occupational Safety and Health (NIOSH) under grant 200-2016-90154. The authors would like to extend their gratitude for the financial support. Special thanks to Mark K. Larson and Bo-Hyun Kim for reviewing this manuscript prior to submission and providing valuable suggestions. Interested readers can obtain the data pertaining to this research article from https://figshare.com/s/5a08eb7a6855be5fa527

References

Abdelaziz, A., Zhao, Q., & Grasselli, G. (2018). Grain based modelling of rocks using the combined finite-discrete element method. *Computers and Geotechnics*, *103*, 73–81.

Alejano, L. R., & Alonso, E. (2005). Considerations of the dilatancy angle in rocks and rock masses. *International Journal of Rock Mechanics and Mining Sciences*, *42*, 481–507.

Arzúa, J., & Alejano, L. R. (2013). Dilation in granite during servo-controlled triaxial strength tests. *International Journal of Rock Mechanics and Mining Sciences*, *61*, 43–56.

Bai, Q., Tu, S., Zhang, C., & Zhu, D. (2016). Discrete element modeling of progressive failure of wide coal roadway from water-rich roofs. *International Journal of Coal Geology*, *167*, 215–229.

Bass, J. D. (1995). Elasticity of minerals, glasses, and melts. *Mineral physics and crystallography: A handbook of physical constants*, *2*, 45–63.

Bieniawski, Z. T. (1967). Mechanism of brittle fracture of rock: Part I—Theory of the fracture process. *International Journal of Rock Mechanics and Mining Sciences and Geomechanical Abstracts*, *4*(4), 395–406.

Bieniawski, Z. T. (1968). Fracture dynamics of rock. *International Journal of Fracture Mechanics*, *4*(4), 415–430.

Blair, S. C., & Cook, N. G. W. (1998a). Analysis of compressive fracturein rock using statistical techniques: Part I. A non-linear rule-based model. *International Journal of Rock Mechanics and Mining Sciences*, *35*, 837–848.

Blair, S. C., & Cook, N. G. W. (1998b). Analysis of compressive fracture in rock using statistical techniques: Part II. Effect of microscale heterogeneity on macroscopic deformation. *International Journal of Rock Mechanics and Mining Sciences*, *35*, 849–861.

Bourcier, M., Bornert, M., Dimanov, A., Héripré, E., & Raphanel, J. L. (2013). Multiscale experimental investigation of crystal plasticity and grain boundary sliding in synthetic halite using digital image correlation. *Journal of Geophysical Research: Solid Earth*, *118*, 511–526. https://doi.org/10.1002/jgrb.50065

Brace, W. F., Paulding, W. B., & Scholz, C. (1966). Dilatancy in the fracture of crystalline rocks. *Journal of Geophysical Research*, *71*(16), 3939–3953.

Chandler, N. A. (2013). Quantifying long-term strength and rock damage properties from plots of shear strain versus volume strain. *International Journal of Rock Mechanics and Mining Sciences*, *59*, 105–110.

Chen, S., Yue, Z. Q., & Tham, L. G. (2007). Digital image based approach for three-dimensional mechanical analysis of heterogeneous rocks. *Rock Mechanics and Rock Engineering*, *40*(2), 145.

Chen, W., & Konietzky, H. (2014). Simulation of heterogeneity, creep, damage and lifetime forloaded brittle rocks. *Tectonophysics*, *633*, 164–175.

Chen, W., Konietzky, H., Tan, X., & Frühwirt, T. (2016). Pre-failure damage analysis for brittle rocks under triaxial compression. *Computers and Geotechnics*, *74*, 45–55.

Christianson, M., Board, M., & Rigby, D. (2006). UDEC simulation of triaxial testing of lithophysal tuff. Proceedings of *41st US Symposium on Rock Mechanics*.

Chu, T. C., Ranson, W. F., & Sutton, M. A. (1985). Applications of digital-image-correlation techniques to experimental mechanics. *Experimental Mechanics*, *25*(3), 232–244.

Cundall, P. A. (1971). A computer model for simulating progressive large-scale movements in blocky rock systems. Proceedings of Int. Society for Rock Mechanics Symposium: Rock Fracture, 129–136.

Dey, T. N., & Wang, C. Y. (1981). Some mechanisms of microcrack growth and interaction in compressive rock failure. *International Journal of Rock Mechanics and Mining Sciences*, *18*, 199–209.

Diederichs, M. S. (1999). *Instability of hard rock masses: The role of tensile damage and relaxation [Ph. D. Thesis]*. Waterloo: University of Waterloo.

Diederichs, M. S. (2003). Rock fracture and collapse under low confinement conditions. *Rock Mechanics and Rock Engineering*, *36*(5), 339–381.

Diederichs, M. S. (2007). The 2003 Canadian Geotechnical Colloquium: Mechanistic interpretation and practical application of damage and spalling prediction criteria for deep tunnelling. *Canadian Geotechnical Journal*, *44*(9), 1082–1116.

Diederichs, M. S., Kaiser, P. K., & Eberhardt, E. (2004). Damage initiation and propagation in hard rock during tunnelling and the influence of near-face stress rotation. *International Journal of Rock Mechanics and Mining Sciences*, *41*(5), 785–812.

Diederichs, M. S., & Martin, C. D. (2010). Measurement of spalling parameters from laboratory testing. In J. Zhao, V. Labiouse, J. P. Dudt, & J. F. Mathiereds (Eds.), *Rock Mechanics in Civil and Environmental Engineering* (pp. 323–326). London: Taylor & Francis.

Eberhardt, E., Stead, D., Stimpson, B., & Read, R. S. (1998). Identifying crack initiation and propagation thresholds in brittle rock. *Canadian Geotechnical Journal*, *35*(2), 222–233.

Eberhardt, E., Stimpson, B., & Stead, D. (1999). The influence of mineralogy on the initiation of microfractures in granite. Proceedings of the *9th ISRM Congress*.

Edelbro, C. (2009). Numerical modelling of observed fallouts in hard rock masses using an instantaneous cohesion-softening friction-hardening model. *Tunnelling and Underground Space Technology*, *24*, 398–409.

Fabjan, T., Mas Ivars, D., & Vukadin, V. (2015). Numerical simulation of intact rock behaviour via the continuum and Voronoi tesselletion models: A sensitivity analysis. *Acta Geotechnica Slovenica*, *12*(2), 5–23.

Fairhurst, C., & Cook, N. G. W. (1966). The phenomenon of rock splitting parallel to the direction of maximum compression in the neighborhood of a surface. Proceedings of *1st Congress, Int. Soc. of Rock Mech*., Lisbon.

Farahmand, K., & Diederichs, M. S. (2015). A calibrated synthetic rock mass (SRM) model for simulating crack growth in granitic rock considering grain scale heterogeneity of polycrystalline rock. Proceedings of *49th US Rock Mechanics/Geomechanics Symposium*.

Farahmand, K., Vazaios, I., Diederichs, M. S., & Vlachopoulos, N. (2018). Investigating the scale-dependency of the geometrical and mechanical properties of a moderately jointed rock using a synthetic rock mass (SRM) approach. *Computers and Geotechnics*, *95*, 162–179.

Gallagher, J. J., Friedman, M., Handin, J., & Sowers, G. M. (1974). Experimental studies relating to microfracture in sandstone. *Tectonophysics*, *21*, 203–247.

Gao, F., Stead, D., & Elmo, D. (2016). Numerical simulation of microstructure of brittle rock using a grain-breakable distinct element grain-based model. *Computers and Geotechnics*, *78*, 203–217.

Gao, F. Q., & Stead, D. O. (2014). The application of a modified Voronoi logic to brittle fracture modelling at the laboratory and field scale. *International Journal of Rock Mechanics and Mining Sciences*, *68*, 1–14.

Ghazvinian, E. (2015). Fracture initiation and propagation in low porosity crystalline rocks: Implications for excavation damage zone (EDZ) mechanics. PhD Thesis, Queen's University, Canada.

Ghazvinian, E., Diederichs, M. S., & Quey, R. (2014). 3D random Voronoi grain-based models for simulation of brittle rock damage and fabric-guided micro-fracturing. *Journal of Rock Mechanics and Geotechnical Engineering*, *6*(6), 506–521.

Haimson, B., & Chang, C. (2000). A new true triaxial cell for testing mechanical properties of rock, and its use to determine rock strength and deformability of Westerly granite. *International Journal of Rock Mechanics and Mining Sciences*, *37*(1–2), 285–296.

Hajiabdolmajid, V., Kaiser, P. K., & Martin, C. D. (2002). Modelling brittle failure of rock. *International Journal of Rock Mechanics and Mining Sciences*, *39*(6), 731–341.

Hedayat, A., Pyrak-Nolte, L. J., & Bobet, A. (2014). Detection and quantification of slip along non-uniform frictional discontinuities using digital image correlation. *Geotechnical Testing Journal*, *37*(5), 786–799.

Hoek, E., Carranza-Torres, C., & Corkum, B. (2002). Hoek-Brown failure criterion-2002 edition. *Proceedings of NARMS-Tac*, *1*(1), 267–273.

Hofmann, H., Babadagli, T., Yoon, J. S., Zang, A., & Zimmermann, G. (2015). A grain based modeling study of mineralogical factors affecting strength, elastic behavior and micro fracture development during compression tests in granites. *Engineering Fracture Mechanics*, *147*, 261–275.

Hudson, J., Harrison, J., & Popescu, M. (2002). Engineering rock mechanics: An introduction to the principles.

Itasca. (2014). UDEC Version 6.0: Theory and background. Itasca Consulting Group Inc., Minneapolis, Minnesota.

Kazerani, T., & Zhao, J. (2010). Micromechanical parameters in bonded particle method for modelling of brittle material failure. *International Journal for Numerical and Analytical Methods in Geomechanics*, *34*(18), 1877–1895.

Lajtai, E. Z. (1998). Microscopic fracture processes in a granite. *Rock Mechanics and Rock Engineering*, *31*, 237–250.

Lan, H., Martin, C. D., & Hu, B. (2010). Effect of heterogeneity of brittle rock on micromechanical extensile behavior during compression loading. *Journal of Geophysical Research*, *115*, B01202. https://doi.org/10.1029/2009JB006496

Lee, S. E., Kim, M. I., Park, J. H., Park, C. K., Kang, M., & Jeong, G. C. (2006). Damage process of intact granite under uniaxial compression: Microscopic observations and contact stress analysis of grains. *Geosciences Journal*, *10*(4), 457–463.

Li, D., Zhu, Q., Zhou, Z., Li, X., & Ranjith, P. G. (2017). Fracture analysis of marble specimens with a hole under uniaxial compression by digital image correlation. *Engineering Fracture Mechanics*, *183*, 109–124.

Li, J., Konietzky, H., & Frühwirt, T. (2017). Voronoi-based DEM simulation approach for sandstone considering grain structure and pore size. *Rock Mechanics and Rock Engineering*, *50*(10), 2749–2761.

Li, L., Lee, P. K., Tsui, Y., Tham, L. G., & Tang, C. A. (2003). Failure process of granite. *International Journal of Geomechanics*, *3*(1), 84–98.

Li, X. F., Li, H. B., & Zhao, J. (2019). The role of transgranular capability in grain-based modelling of crystalline rocks. *Computers and Geotechnics*, *110*, 161–183.

Lin, Q., & Labuz, J. F. (2013). Fracture of sandstone characterized by digital image correlation. *International Journal of Rock Mechanics and Mining Sciences*, *60*, 235–245.

Liu, G., Cai, M., & Huang, M. (2018). Mechanical properties of brittle rock governed by micro-geometric heterogeneity. *Computers and Geotechnics*, *104*, 358–372.

Mahabadi, O. K. (2012). Investigating the influence of micro-scale heterogeneity and microstructure on the failure and mechanical behaviour of geomaterials. PhD Thesis, University of Toronto, Canada.

Mair, K., Elphick, S., & Main, I. (2002). Influence of confining pressure on the mechanical and structural evolution of laboratory deformation bands. *Geophysical Research Letters*, *29*(10), 1410. https://doi.org/10.1029/2001GL013964

Martin, C. D., & Chandler, N. A. (1994). The progressive fracture of Lac du Bonnet granite. *International Journal of Rock Mechanics and Mining Science and Geomechanics Abstracts*, *31*(6), 643–659.

Mavko, G., Mukerji, T., & Dvorkin, J. (2009). *The rock physics handbook: Tools for seismic analysis of porous media*. Cambridge: Cambridge University Press.

Munjiza, A. A. (2004). *The Combined Finite-Discrete Element Method*. New York: John Wiley & Sons.

Nasseri, M. H., & Mohanty, B. (2008). Fracture toughness anisotropy in granitic rocks. *International Journal of Rock Mechanics and Mining Sciences*, *45*(2), 167–193.

Nicksiar, M., & Martin, C. D. (2012). Evaluation of methods for determining crack initiation in compression tests on low-porosity rocks. *Rock Mechanics and Rock Engineering*, *45*(4), 607–617.

Noorani, R., & Cai, M. (2015). Simulation of dilation behavior of brittle rocks using a grain-based model. Proceedings of *13th ISRM International Congress of Rock Mechanics*.

Pan, B., Qian, K., Xie, H., & Asundi, A. (2009). Two-dimensional digital image correlation for in-plane displacement and strain measurement: A review. *Measurement Science and Technology*, *20*(6), 062001.

Pan, B., Xie, H. M., Guo, Z. Q., & Hua, T. (2007). Full-field strain measurement using a two-dimensional Savitzky–Golay digital differentiator in digital image correlation. *Optics and Lasers in Engineering*, *46*, 033601.

Park, J. W., Park, C., Song, J. W., Park, E. S., & Song, J. J. (2017). Polygonal grain-based distinct element modeling for mechanical behavior of brittle rock. *International Journal for Numerical and Analytical Methods in Geomechanics*, *41*(6), 880–898.

Patel, S., & Martin, C. D. (2018). Evaluation of tensile Young's modulus and Poisson's ratio of a bi-modular rock from the displacement measurements in a Brazilian test. *Rock Mechanics and Rock Engineering*, *51*(2), 361–373.

Paterson, M. S., & Wong, T. F. (2005). *Experimental rock deformation-the brittle field*. New York: Springer Science & Business Media.

Peng, J., Wong, L. N., The, C. I., & Li, Z. (2018). Modeling micro-cracking behavior of Bukit Timah granite using grain-based model. *Rock Mechanics and Rock Engineering*, *51*(1), 135–154.

Peng, S., & Johnson, A. M. (1972). Crack growth and faulting in cylindrical specimens of Chelmsford granite. *International Journal of Rock Mechanics and Mining Science and Geomechanics Abstracts*, *9*(1), 37–86.

Perras, M. A., & Diederichs, M. S. (2014). A review of the tensile strength of rock: Concepts and testing. *Geotechnical and Geological Engineering*, *32*(2), 525–546.
Rahjoo, M., & Eberhardt, E. (2016). A simplified dilation model for modeling the inelastic behavior of rock. Proceedings of *50th US Rock Mechanics/Geomechanics Symposium*.
Schwartz, E., Saralaya, R., Cuadra, J., Hazeli, K., Vanniamparambil, P. A., Carmi, R., & Kontsos, A. (2013). The use of digital image correlation for non-destructive and multi-scale damage quantification. In: *Sensors and Smart Structures Technologies for Civil, Mechanical, and Aerospace Systems 2013*, International Society for Optics and Photonics, 8692, 86922H.
Shirole, D., Hedayat, A., & Walton, G. (2019). Experimental relationship between compressional wave attenuation and surface strains in brittle rock. *Journal of Geophysical Research: Solid Earth*, *124*, 5770–5793. https://doi.org/10.1029/2018JB017086
Shirole, D., Hedayat, A., & Walton, G. (2020). Experimental investigation of multi-scale strain-field heterogeneity in rocks. *International Journal of Rock Mechanics and Mining Sciences*, *127*, 104212.
Sinha, S., & Walton, G. (2019). Simulating laboratory-scale damage in granite using bonded block models (BBM). Proceedings of *14th International Congress on Rock Mechanics and Rock Engineering*, Brazil.
Sinha, S., & Walton, G. (2020). A study on bonded block model (BBM) complexity for simulation of laboratory-scale stress-strain behavior in granitic rocks. *Computers and Geotechnics*, *118C*, 103363.
Sprunt, E. S., & Brace, W. F. (1974). Direct observation of microcavities in crystalline rocks. *International Journal of Rock Mechanics and Mining Science and Geomechanics Abstracts*, *11*(4), 139–150.
Stavrou, A., & Murphy, W. (2018). Quantifying the effects of scale and heterogeneity on the confined strength of micro-defected rocks. *International Journal of Rock Mechanics and Mining Sciences*, *102*, 131–143.
Sutton, M. A., Orteu, J. J., & Schreier, H. (2009). *Image correlation for shape, motion and deformation measurements: Basic concepts, theory and applications*. USA: Springer Science & Business Media.
Tan, X., Konietzky, H., & Chen, W. (2016). Numerical simulation of heterogeneous rock using discrete element model based on digital image processing. *Rock Mechanics and Rock Engineering*, *49*(12), 4957–4964.
Tan, X., Konietzky, H., & Frühwirt, T. (2015). Numerical simulation of triaxial compression test for brittle rock sample using a modified constitutive law considering degradation and dilation behavior. *Journal of Central South University*, *22*(8), 3097–3107.
Tapponnier, P., & Brace, W. F. (1976). Development of stress-induced microcracks in westerly granite. *International Journal of Rock Mechanics and Mining Science and Geomechanics Abstracts*, *13*(4), 103–112.
Tung, S. H., Shih, M. H., & Sung, W. P. (2008). Development of digital image correlation method to analyse crack variations of masonry wall. *Sadhana*, *33*(6), 767–779.
Turichshev, A., & Hadjigeorgiou, J. (2017). Development of synthetic rock mass bonded block models to simulate the behaviour of intact veined rock. *Geotechnical and Geological Engineering*, *35*(1), 313–335.
Vardoulakis, I. (1980). Shear band inclination and shear modulus of sand in biaxial tests. *International Journal for Numerical and Analytical Methods in Geomechanics*, *4*, 103–119.
Vermeer, P. A., & De Borst, R. (1984). Non-associated plasticity for soils, concrete and rock. *HERON*, *29*(3).
Villeneuve, M., Diederichs, M., & Kaiser, P. (2012). Effects of grain scale heterogeneity on rock strength and the chipping process. *International Journal of Geomechanics*, *12*, 632–647.
Villeneuve, M. C. (2008). Examination of geological influence on machine excavation of highly stressed tunnels in massive hard rock. PhD thesis, Queen's University, Kingston, Canada.
Villeneuve, M. C., Diederichs, M. S., Kaiser, P. K., & Frenzel, C. (2009). Constitutive model for numerical modelling of highly stressed heterogeneous massive rocks at excavation boundaries. Proceedings of *3rd Canada-USA Rock Mechanics Symposium*, Toronto, Canada.
Villeneuve, M. C., & Siratovich, P. A. (2015). Experimental and numerical modelling of thermal stimulation in geothermal core studies. Proceedings of the *13th ISRM International Congress of Rock Mechanics*, Montreal, Canada.
Walton, G. (2014). Improving continuum models for excavations in rock masses under high stress through an enhanced understanding of post-yield dilatancy. Ph.D. Thesis. Queen's University, Kingston, Canada.
Walton, G. (2018). Scale effects observed in compression testing of Stanstead granite including post-peak strength and dilatancy. *Geotechnical and Geological Engineering*, *36*(2), 1091–1111.
Walton, G., Diederichs, M., Punkkinen, A., & Whitmore, J. (2016). Back analysis of a pillar monitoring experiment at 2.4 km depth in the Sudbury Basin, Canada. *International Journal of Rock Mechanics and Mining Sciences*, *85*, 33–51.
Walton, G., & Diederichs, M. S. (2015a). A new model for the dilation of brittle rocks based on laboratory compression test data with separate treatment of dilatancy mobilization and decay. *Geotechnical and Geological Engineering*, *33*(3), 661–679.
Walton, G., & Diederichs, M. S. (2015b). A mine shaft case study on the accurate prediction of yield and displacements in stressed ground using lab-derived material properties. *Tunnelling and Underground Space Technology*, *49*, 98–113.
Walton, G., Hedayat, A., Kim, E., & Labrie, D. (2017). Post-yield strength and dilatancy evolution across the brittle–ductile transition in Indiana limestone. *Rock Mechanics and Rock Engineering*, *50*(7), 1691–1710.
Wang, X., & Cai, M. (2018). Modeling of brittle rock failure considering inter-and intra-grain contact failures. *Computers and Geotechnics*, *101*, 224–244.
Wang, X., & Cai, M. (2019). A comprehensive parametric study of grain-based models for rock failure process simulation. *International Journal of Rock Mechanics and Mining Sciences*, *115*, 60–76.
Wawersik, W. R., & Brace, W. F. (1971). Post-failure behavior of a granite and diabase. *Rock Mechanics*, *3*(2), 61–85.
Wong, T. F. (1982). Micromechanics of faulting in Westerly Granite. *International Journal of Rock Mechanics and Mining Sciences*, *19*, 49–64.
Wong, T. F., Wong, R. H. C., Chau, K. T., & Tang, C. A. (2006). Microcrack statistics, Weibull distribution and micromechancial modeling of compressive failure in rock. *Mechanics of Materials*, *38*, 664–681.
Wulff, A. M., Hashida, T., Watanabe, K., & Takahashi, H. (1999). Attenuation behaviour of tuffaceous sandstone and granite during microfracturing. *Geophysical Journal International*, *139*(2), 395–409.
Xing, H. Z., Zhang, Q. B., Ruan, D., Dehkhoda, S., Lu, G. X., & Zhao, J. (2018). Full-field measurement and fracture characterisations of rocks under dynamic loads using high-speed three-dimensional digital image correlation. *International Journal of Impact Engineering*, *113*, 61–72.
Zhao, X. G., & Cai, M. (2010). A mobilized dilation angle model for rocks. *International Journal of Rock Mechanics and Mining Sciences*, *47*(3), 368–384.
Zhao, X. G., Cai, M., & Cai, M. (2010). Considerations of rock dilation on modeling failure and deformation of hard rocks—A case study of the mine-by test tunnel in Canada. *Journal of Rock Mechanics and Geotechnical Engineering*, *2*, 338–349.

Zhou, J., Lan, H., Zhang, L., Yang, D., Song, J., & Wang, S. (2019). Novel grain-based model for simulation of brittle failure of Alxa porphyritic granite. *Engineering Geology*, *251*, 100–114.

Zhou, X. P., Lian, Y. J., Wong, L. N., & Berto, F. (2018). Understanding the fracture behavior of brittle and ductile multi-flawed rocks by uniaxial loading by digital image correlation. *Engineering Fracture Mechanics*, *199*, 438–460.

Zhu, W. C., & Tang, C. A. (2004). Micromechanical model for simulating the fracture process of rock. *Rock Mechanics and Rock Engineering*, *37*(1), 25–56.